1 **The story of a summit nucleus:**

2 **Hillslope boulders and their effect on erosional patterns and landscape morphology**

3 **in the Chilean Coastal Cordillera**

4 Emma Lodes[1*], Dirk Scherler[1,2], Renee van Dongen,[3] and Hella Wittmann[1]

5 [1]GFZ German Research Centre for Geosciences, Earth Surface Geochemistry, Telegrafenberg,

6 14473 Potsdam, Germany

7 [2]Freie Universität Berlin, Institute of Geographical Sciences, 12249 Berlin, Germany

8 [3]International Centre for Water Resources and Global Change, 56068 Koblenz, Germany

9 *Corresponding author (lodes@gfz-potsdam.de)

10

13

14 **Abstract**

15   While landscapes are broadly sculpted by tectonics and climate, on a catchment scale,

16 sediment size can regulate hillslope denudation rates and thereby influence the location of

17 topographic highs and valleys. In this work, we used *in situ* [10]Be cosmogenic radionuclide

18 analysis to measure the denudation rates of bedrock, boulders, and soil, in three granitic

19 landscapes with different climates in Chile. We hypothesize that bedrock and boulders affect

20 differential denudation by denuding more slowly than the surrounding soil, where the null

21 hypothesis is that no difference exists between soil and boulder or bedrock denudation rates. To

22 evaluate denudation rates, we present a simple model that assesses differential denudation of

23   boulders and the surrounding soil by evaluating boulder protrusion height against a two-stage

24   erosion model and measured ^{10}Be concentrations of boulder tops. We found that hillslope

25   bedrock and boulders consistently denude more slowly than soil in two out of three of our field

26   sites, which have a humid and a semi-arid climate: denudation rates range from ~5 to 15 m Myr^{-1}

27   for bedrock and boulders and from ~8 to 20 m Myr^{-1} for soil. Furthermore, across a bedrock ridge

28   in the humid site, denudation rates increase with increasing fracture density. In our lower-sloping

29   field sites, boulders and bedrock appear to be similarly immobile based on similar ^{10}Be

30   concentrations. However, in the site with a mediterranean climate, steeper slopes allow for higher

31   denudation rates for both soil and boulders (~40-140 m Myr^{-1}), while the bedrock denudation rate

32   remains low (~22 m Myr^{-1}). Our findings suggest that unfractured bedrock patches and large

33   hillslope boulders affect landscape morphology by inducing differential denudation in lower-

34   sloping landscapes. When occurring long enough, such differential denudation should lead to

35   topographic highs and lows controlled by bedrock exposure and hillslope sediment size, both a

36   function of fracture density. We further examined our field sites for fracture control on landscape

37   morphology by comparing fracture, fault and stream orientations, with the hypothesis that

38   bedrock fracturing leaves bedrock more susceptible to denudation. Similar orientations of

39   fractures, faults, and streams further supports the idea that tectonically-induced bedrock

40   fracturing guides fluvial incision and accelerates denudation through reducing hillslope sediment

41   size.

42   **1   Introduction**

43   Landscapes on Earth are shaped by tectonic uplift and climate, which dictate erosional

44   and weathering regimes over geologic timescales. When uplift and climate are held constant

45   sufficiently long, fluvial landscapes reach a steady state, in which the slopes of hills and stream

46   channels adjust so that denudation rates match tectonic uplift rates (e.g. Burbank et al., 1996;

47   Kirby and Whipple, 2012). Variations in bedrock strength and the grain size of hillslope

48   sediment, however, exert additional control on the morphology of hills and valleys (e.g. Attal et

49   al., 2015; Glade et al., 2017). Initially, hillslope sediment size is set by lithology and the density

50   of fractures, which are formed due to tectonic and topographic stresses (e.g. Molnar et al., 2007;

51   St. Claire et al., 2015; Roy et al., 2016; Sklar et al., 2017). Near the earth surface, water, often

52   carrying biotic acids, infiltrates bedrock fractures and promotes chemical weathering that further

53   reduces sediment size and converts bedrock to regolith (Lebedeva and Brantley, 2017; Hayes et

54   al., 2020). Therefore, long residence times of sediment in the weathering zone (on a million-year

55   timescale) may result in complete disintegration of bedrock and the formation of saprolite and

56   soil, whereas rapid erosion and short residence times can lead to hillslope sediment size limited

57   by fracture spacing (e.g. Attal et al., 2015; Sklar et al., 2017; Roda-Boluda et al., 2018; Verdian et

58   al., 2021). A spectrum between these end-members can also exist within one catchment,

59   especially where variations in lithology, fracture density or elevation cause spatial differences in

60   the rate and/or extent of weathering (e.g. Sklar et al., 2020). Where weathering does not

61   completely disintegrate the bedrock, boulders, or corestones, can be found embedded in hillslope

62   sediment, with a maximum size set by the spacing of bedrock fractures (Fletcher and Brantley,

63   2010; Buss et al., 2013; Sklar et al., 2017). Here we focus on the effects of such boulders on

64   differential denudation and landscape morphology on hillslopes with mixed cover of soil,

65   boulders and bedrock.

66   Soil-mantled hillslopes are typically considered to be dominated by diffusive processes,

67   for which conceptual models and geomorphic transport laws are relatively well-established (e.g.,

68   Dietrich et al., 2003; Perron, 2011). However, these models generally assume uniform hillslope

69   material and do not account for the exhumation of larger boulders through the critical zone. Neely

70   et al. (2019) recently addressed erosion and soil transport on mixed bedrock and soil-covered

71   hillslopes using a nonlinear diffusion model, but assumed the same denudation rate for bedrock

72   and soil. Fletcher and Brantley (2010) modeled the reduction in the size of corestones due to

73   chemical weathering as they are exhumed through the weathering zone, although this model does

74   not consider the corestones' effect on differential erosion. Often, however, bedrock and large

75   boulders protrude above the surrounding soil, indicating that they are eroding more slowly than

76   the soil (Biermann and Caffee, 2002). Indeed, studies have shown that average denudation rates

77   of bedrock outcrops and hillslope boulders are often lower than catchment average and soil

78   denudation rates (e.g. Bierman, 1994; Heimsath et al., 2000; Heimsath et al., 2001; Granger et al.,

79   2001; Portenga and Bierman, 2011).

80   Larger boulders require greater forces to be moved, which can be achieved by steepening

81   slopes (Granger et al., 2001; DiBiase et al., 2018; Neely and DiBiase, 2020), or by lengthening

82   residence time until subaerial weathering has decreased their size sufficiently to be transported

83   downslope. During this prolonged residence time, boulders can shield hillslopes from erosion

84   (Glade et al., 2017; Chilton and Spotlia, 2020), and stream channels from incision (Shobe et al.,

85   2016; Thaler and Covington, 2016). In terrain where spatial gradients in bedrock fracture spacing

86   result in spatial gradients of hillslope sediment size, it is thus reasonable to expect that the

87   resistance of surface boulders to weathering and transport ought to retard erosion locally,

88   resulting in spatially differential erosion. Moreover, fractured, and therefore weaker, bedrock

89   facilitates erosion via both abrasion and plucking by streams (Lamb et al., 2015; Sklar and

90   Dietrich, 2011), and smaller blocks are also more easily transported in fluvial systems (Shobe et

91   al., 2016). Therefore, we would expect that rivers preferentially incise in zones of more intensely

92   fractured rocks (Buss et al., 2013) that align with the orientation of faults (Molnar et al., 2007;

93   Roy et al., 2016).

94   In this study we provide a new framework for measuring and assessing differential

95   denudation of boulders and the surrounding fine-grained regolith on hillslopes, and also discuss

96   the extent to which bedrock fracturing affects sediment size, denudation rates, and stream

97   incision. We quantified bedrock, boulder, and soil denudation rates in three different areas along

98   the granitic Coastal Cordillera of Chile with different climates and erosional regimes, using *in*

99   *situ* cosmogenic ^{10}Be. By developing a simple model to convert ^{10}Be concentrations from

100   boulders into soil and boulder denudation rates, we explored the hypothesis that on a hillslope,

101   boulders affect differential erosion by eroding more slowly than the surrounding soil, with the

102   corresponding null hypothesis that no difference exists between soil and boulder denudation rates.

103   We make the simplifying assumption that soil denudation rates remain constant over the time

104   period that a boulder is exhumed, and over long time periods, denudation rates throughout the

105   landscape vary according to whether boulders or soil are exposed at the surface. Following the

106   logic outlined above, we additionally examined our field sites for signs of fracture control on

107   landscape morphology with the hypothesis that more highly fractured bedrock is more susceptible

108   to denudation and stream incision than intact bedrock.

109   **2   Field sites**

110   The Chilean Coastal Cordillera, a series of batholiths in the forearc of the Andean

111   subduction zone, lies along a marked climate gradient with humid conditions in the south and

112   hyper-arid conditions in the north (Fig. 1). The Andean subduction zone, in which the Nazca

113   Plate subducts under the South American Plate, has been active since at least Jurassic times (e.g.,

114   Coira et al., 1982). In this study we investigated three field sites along the Coastal Cordillera from

115   south to north: Nahuelbuta National Park, (NA), with a humid-temperate climate, La Campana

116   National Park (LC), with a mediterranean climate, and Private Reserve Santa Gracia (SG), with a

117   semi-arid climate (Fig. 1). NA and SG have more gently-sloping hillslopes with a lack of

118   observed landslides, while hillslopes in LC are steeper and landslides have been observed (van

119   Dongen et al., 2019; Terweh et al., 2021). All three sites are underlain by granitoid bedrock

120   (Oeser et al., 2018), none show any signs of former glaciation, and all are located on protected

121   land, away from major human influence, such as mines, dams, and large infrastructure. In all

122   three sites, denudation rates from ^{10}Be cosmogenic radionuclide analysis have been reported by

123   van Dongen et al. (2019) (catchment average rates), and Schaller et al. (2018) (soil pits).

124   NA is located on an uplifted, fault-bounded block (plateau), an unusually high part of the

125   Coastal Cordillera with a mean elevation of ~1300 m above sea level. Tectonic uplift rates in NA

126   increased from 0.03–0.04 to >0.2 mm year^{-1} at 4±1.2 Ma (Glodny et al., 2008), a shift that

127   appears to be also recorded by knickpoints in streams that drain the plateau. All of the

128   measurements in this work are from the plateau (~9° mean slope), above knickpoints (see Fig.

129   S1). ^{10}Be-derived denudation rates are around 30 m Myr^{-1} (Schaller et al., 2018; van Dongen et

130   al., 2019), indicating that denudation rates on the NA plateau have not yet adjusted to the higher

131   uplift rates. The main catchment in LC has a mean elevation of 1323 m with a mean slope of 23°,

132   and regional uplift rates are estimated to be <0.1 mm yr^{-1} (Melnick, 2016). Van Dongen et al.

133   (2019) reported a catchment average denudation rate of ~200 m Myr^{-1} for a sub-catchment in LC,

134   whereas Schaller et al. (2018) reported soil denudation rates of 40-55 m Myr^{-1}. In SG, the mean

135   elevation is 773 m above sea level, the mean slope is 17.2°, and uplift rates are <0.1 mm year^{-1}

136   (Melnick, 2016). Previously reported ^{10}Be-derived denudation rates are ~9-16 m Myr^{-1} (Schaller

137   et al., 2018; van Dongen et al., 2019).

3 Methods

3.1 In situ [10]Be analysis

3.1.1 Sample collection

138

139

140

141   We collected samples for cosmogenic [10]Be analysis from bedrock, boulders, and soil to

142 estimate denudation rates in our field sites, targeting hillslopes near previously-collected

143 catchment average and soil pit samples from van Dongen et al (2019) and Schaller et al. (2020).

144 All sample locations are shown in Figure 1. Bedrock samples were taken using a hammer and

145 chisel from an area of up to ~20 m × 20 m (on ridge tops or hillslopes) and consist of an

146 amalgamation of at least ten chips (~25 cm^2 and <2 cm thick), with which we aim to obtain

147 representative mean values of denudation rates that are potentially variable due to episodic

148 erosion by spalling rock chips (Small et al., 1997). Similarly, for boulder samples, one chip was

149 taken from the top of each of at least ten similarly-sized boulders and amalgamated for an area of

150 up to ~40 m × 40 m, depending on boulder abundance. Topsoil samples were also collected by

151 amalgamation in the area surrounding the sampled boulders. In places with many various-sized

152 boulders, we collected samples from different protrusion heights (~1-m tall boulders, ~0.5-m tall

153 boulders, etc.). Each sampled boulder was measured along the a, b, and c axes, as far as

154 discernible (see Table 1). We also measured the protrusion height of each boulder from the center

155 of the top of the boulder to the ground. Each protrusion height value in Table 1 consists of an

156 average of at least ten boulders of similar protrusion heights that we sampled for one

157 amalgamated sample. Boulders on sloping surfaces typically show varying protrusion heights,

158 with higher values downslope and lower values upslope. In such cases, we measured protrusion at

159 the sides of boulders. Occasionally, we observed that upslope protrusion was further reduced by

160 sediment trapping upslope of boulders. We targeted boulders that appear to be in situ (essentially,

161   exhumed corestones), based on the observation that they are tightly imbedded in the ground. We

162   acknowledge that it is possible that some of the larger sampled boulders are connected to bedrock

163   roots, and that it is also possible that some boulders are not in situ, despite our best efforts.

164   In NA, we collected five bedrock samples from an area called Piedra de Aguila from

165   outcrops with different fracture densities, and measured fracture spacing (47 measurements) by

166   stringing a measuring tape along the bedrock surface and measuring the distance between

167   fractures that were at least 1 mm wide, and fracture orientations (41 measurements), using a

168   Brunton compass (Fig. 2A1 and 2A2). We further collected six boulder samples and three soil

169   samples from the ridge and hillslope of Cerro Anay (Fig. 2A3), an area called Casa de Piedras,

170   and a hillslope near the soil pits that were sampled by Schaller et al. (2018). We measured the

171   dimensions of all boulders from which we took a sample chip (141 boulders). In LC and SG, we

172   were not able to collect samples at variably fractured bedrock outcrops due to rarely exposed

173   bedrock. In LC, we took one bedrock sample, two boulder samples and two soil samples from the

174   ridge and slope of Cerro Cabra (Fig. 2B1), and three boulder samples and three soil samples from

175   the ridge, upper slope, and lower slope of Cerro Guanaco (Fig. 2B3). In SG, we took four boulder

176   samples and three soil samples from the ridge and slope of Santa Gracia Hill, which also hosts the

177   soil pits of Schaller et al. (2018) (Fig. 2C2 and 2C3), and two boulder samples and one soil

178   sample from the ridge of Zebra Hill (Fig. 2C1).

179   **3.1.2   Analytical methods**

180   We dried, crushed, and sieved amalgamated bedrock and boulder samples for quartz

181   mineral separation, and dried and sieved soils, each to 250-500 micrometer particle size, or to

182   250-1000 micrometers if the 250-500 micrometer sample amount wasn't sufficient. We used

183   standard physical and chemical separation methods to isolate ~20 g of pure quartz from each

184   sample. After spiking each sample with 150 µg of ^{9}Be carrier and dissolving the quartz in

185   concentrated hydrofluoric acid, we extracted Be following protocols adapted from von

186   Blanckenburg et al. (2004). ^{10}Be/^{9}Be$_{(carrier)}$ ratios were measured by accelerator mass

187   spectrometry at the University of Cologne, Germany (Dewald et al., 2013). Sample ratios were

188   normalized to standards KN01-6-2 and KN01-5-3 with ratios of 5.35×10^{-13} and 6.320×10^{-12},

189   respectively. Final ^{10}Be concentrations were corrected by process blanks with an average

190   Be^{10}/Be$^9{}_{(carrier)}$ ratio of $(2.21 \pm 0.25) \times 10^{-14}$.

3.1.3   Denudation rate calculations

191

192   In order to calculate denudation rates from the measured ^{10}Be concentrations, we

193   evaluated bedrock, boulder, and soil samples differently. Bedrock samples present the simplest

194   case, in which we assumed steady state erosion and calculated bedrock denudation rates (ϵ_{br})

195   using the CRONUS online calculator v2.3 (Balco et al., 2008). The steady state assumption is

196   based on our amalgamated sampling, and follows the results of Small et al. (1997), who showed

197   that an amalgamation of several individual bedrock samples is a reasonable approximation of the

198   long-term average denudation rate in episodically eroding settings.

199   Boulder and soil samples require a more nuanced assessment. Boulders protrude above

200   the ground surface, which implies that the lowering of the ground surface (i.e., the soil

201   denudation rate, ϵ_s) is faster than the lowering of the boulder's surfaces (i.e., the boulder

202   denudation rate, ϵ_b) (Fig. 3). Thus, even while they are buried and covered by soil (or saprolite),

203   boulders are exposed to cosmic rays for a significant amount of time prior to breaching the

204   surface (Fig. 3A). We refer to this time span as phase 1. When boulders breach the surface, they

205   should have a concentration similar to that of the surrounding soil (Fig. 3B). As boulders are

206   exposed during phase 2, nuclide production and decay continues, but it takes time for the boulder

207   surfaces to attain a [10]Be concentration that is in equilibrium with the slower boulder denudation

208   rate. Thus, we expect that the measured concentrations from the tops of boulders are

209   combinations of the two different phases in which [10]Be is accumulated at different rates (first a

210   rate corresponding to the soil denudation rate, and after exhumation, a rate corresponding to the

211   boulder denudation rate). Converting the [10]Be concentrations of soil samples collected from

212   around the boulders to a denudation rate also requires a special approach, as these samples

213   include an unknown number of grains eroded off boulders, which ought to increase the [10]Be

214   concentration, due to the slower denudation rate of boulders, as compared to soil.

215   Because of the above complications, we used an approach to estimate the soil and boulder

216   denudation rates that considers the measured boulder protrusion heights and their measured [10]Be

217   concentrations. We modelled [10]Be concentrations ($N_{modelled}$, in atoms g^{-1}) by approximating the

218   production rate profile with a combination of several exponential functions (e.g., Braucher et al.,

219   2011) during the two different phases:

$$N_{modelled} = \sum_i \frac{P_i(0)}{\lambda + \frac{\epsilon_s \rho}{\Lambda_i}} e^{-t_2 \lambda} + \sum_i \frac{P_i(0)}{\lambda + \frac{\epsilon_b \rho}{\Lambda_i}} \left[1 - e^{-t_2 \left(\lambda + \frac{\epsilon_b \rho}{\Lambda_i}\right)} \right] \quad (1),$$

220   where i indicates different terms for the production by spallation, fast muons, and negative

221   muons; $P_i(0)$ are the site-specific [10]Be surface production rates in atoms g^{-1} yr^{-1} for the different

222   production pathways (Table 1); λ is the [10]Be decay constant (4.9975 ×10^{-7}); ϵ_b is the boulder

223   denudation rate (cm yr^{-1}); and Λ_i is the attenuation length scale (160 g cm^{-2} for spallation, 4320 g

224   cm^{-2} for fast muons, and 1500 g cm^{-2} for negative muons, respectively; Braucher et al., 2011). ρ is

225   the bedrock and boulder density, and here we use a value of 2.6 g cm^{-3} for all samples; we discuss

226   the impact of density changes in section 5.1. Surface production rates by spallation are based on a

227   SLHL (sea level high latitude) reference production rate of 4.01 atoms g^{-1} yr^{-1} (Borchers et al.,

228   2016) and the time-constant spallation production rate scaling scheme of Lal (1991) and Stone

10

229 (2000) ('St' in Balco et al., 2008). Surface production rates by both fast and negative muons were

230 obtained using the MATLAB-function 'P_mu_total.m' of Balco et al. (2008). Topographic

231 shielding at each sampling site was calculated with the function 'toposhielding.m' of the

232 TopoToolbox v2 (Schwanghart and Scherler, 2014) and 12.5-meter resolution ALOS PALSAR-

233 derived digital elevation models (DEMs) from the Alaska Satellite Facility.

234   In equation 1, the first term represents phase 1 and the second term represents phase 2,

235 with t_2 being the exposure time of the boulder, calculated from the height of the boulder (z)

236 divided by the difference between the soil denudation rate and the boulder denudation rate:

$$t_2 = \frac{z}{(\epsilon_s - \epsilon_b)} \tag{2}$$

237 For each sample and associated average boulder protrusion height, we modelled ^{10}Be

238 concentrations with equation 1 for different combinations of soil and boulder denudation rates

239 that we allowed to vary between 5 and 50 m Myr^{-1} (NA), between 3 and 50 m Myr^{-1} (SG), and

240 between 10 and 300 m Myr^{-1} (LC), guided by previously published denudation rate estimates

241 (Schaller et al., 2018; van Dongen et al., 2019). We consider permissible denudation rates as

242 those for which the difference between the modelled and observed ^{10}Be concentrations is less

243 than the measured 2σ concentration uncertainty.

244   This idealized model rests on several assumptions; (1) the landscapes are in a long-term

245 steady state where denudation is locally variable as boulders and bedrock are exhumed in

246 different locations, but this variation is around a long-term stable average; (2) soil denudation

247 rates remain steady over the course of boulder exhumation; (3) boulders are in situ and have not

248 rolled downhill; (4) boulders have not been intermittently shielded during their exhumation; and

249 (5) soil density is inconsequential and can be assigned the same value as bedrock. Assumption 3

250 has a higher chance of being violated on steep slopes or where boulders are tall, and assumption 4

251 is more likely violated where boulders are densely clustered. These assumptions are discussed in

252 more detail in section 5.1.

3.2 Topographic analysis

254 To test if stream orientations in our field sites follow fault orientations, we analyzed the

255 orientations of streams using one-meter resolution LiDAR DEMs (Kügler et al., 2022). Within

256 each DEM, we first calculated stream networks based on flow accumulation area thresholds of

257 10^4, 10^5 and 10^6 m^2. The lowest threshold was determined based on the occurrence of incised

258 channels visible in the DEMs. We then used the TopoToolbox function 'orientation' with a

259 default smoothing factor (K) of 100, to obtain the orientation of each node in the stream network.

260 Fractures in the field can only be seen where there are bedrock outcrops, which are generally

261 scarce. Therefore, we decided to refer to the orientation of faults, as depicted in geological maps,

262 with the assumption of similar orientation (Krone et al., 2021; Rodriguez Padilla et al., 2022). To

263 obtain the orientation of mapped faults, we extracted faults within ~50 km of each sampling site

264 from a 1:1,000,000-scale geological map from Chile's National Geology and Mining Service in

265 ArcGIS (SERNAGEOMIN, 2003). Fault orientations were measured for straight fault segments

266 with a length of 100 m. Because we are only interested in the strike of streams and faults, all

267 orientations lie between 0° and 180°. For displaying purposes in rose diagrams, we mirrored these

268 values around the diagram origin by duplicating values and adding 180°.

4 Results

4.1 [10]Be concentrations

271 Measured [10]Be concentrations span a wide range of values, and are generally lowest in LC

272 and higher in NA and SG (Table 1). Within NA, we observe the lowest averaged [10]Be

273   concentrations (normalized to SLHL) for soil samples ($\mu \pm 2\sigma = 1.41\times10^5\pm0.06\times10^5$ atoms g^{-1}),

274   followed by bedrock samples ($2.19\times10^5\pm0.07\times10^5$ atoms g^{-1}) and boulder samples

275   ($2.82\times10^5\pm0.08\times10^5$ atoms g^{-1}) (Fig. 4A). In NA at Piedra de Aguila, where we were able to

276   measure fracture spacing in areas with exposed bedrock, the ^{10}Be concentrations of samples from

277   fractured bedrock decrease with increasing fracture density (Fig. 5A). One boulder sample from

278   the slope of Soil Pit Hill stands out with a concentration that is lower than most soil samples.

279   Similar, but slightly higher average values as in NA are attained in SG, with soil samples

280   ($2.24\times10^5 \pm 0.11\times10^5$ atoms g^{-1}) being lower than boulder samples ($4.22\times10^5 \pm 0.16\times10^5$ atoms g^{-}

281   ^{1}) (Fig. 4C). Only in LC are the differences between averaged soil ($0.82\times10^5 \pm 0.04\times10^5$ atoms g^{-}

282   ^{1}) and boulder samples ($0.74\times10^5 \pm 0.05\times10^5$ atoms g^{-1}) small, and with 2σ error, within

283   uncertainties (Fig. 4B). In addition, at 3 out of 5 sampling locations in LC, boulders have lower

284   concentrations than adjacent soil samples, inconsistent with the assumption that $\epsilon_s < \epsilon_b$ (see

285   section 3.1.3). However, our single bedrock sample from LC has a higher concentration of

286    $1.38\times10^5 \pm 0.16\times10^5$ atoms g^{-1}. In NA and SG, boulder samples from slope locations have lower

287   average ^{10}Be concentrations compared to boulder samples from ridge locations. Again, in LC this

288   pattern does not hold. Finally, we do not observe a significant trend between ^{10}Be concentration

289   and protrusion height (Fig. 5D); however, there is a relationship between protrusion height and

290   slope for LC (Fig. 5E).

291   **4.2   Bedrock, boulder, and soil denudation rates**

292   Bedrock denudation rates in NA range from 8.53±0.60 m Myr^{-1} to 18.64±1.40 m Myr^{-1},

293   and the LC bedrock sample yielded a denudation rate of 22.28±2.62 m Myr^{-1}. We modelled

294   boulder (ϵ_s) and soil denudation rates (ϵ_s) using the approach described in section 3.1.3 for all

295   boulder samples that have higher concentrations than the adjacent soil concentrations. We address

13

296   locations where ^{10}Be concentrations are higher in soil compared to boulder samples in the

297   discussion (three locations in LC and one in NA). In contrast to the bedrock denudation rates,

298   modelled boulder and soil denudation rates have no unique solution, and their ranges of possible

299   denudation rates are more complex (Fig. 6). The ranges of denudation rates, illustrated by the

300   curves in Fig. 6, are comprised of values for which the difference between the measured and

301   modelled ^{10}Be concentrations are less than the measured 2σ ^{10}Be concentration uncertainty,

302   where modelled ^{10}Be concentrations are based on Eq. 1. Each colored band represents one

303   amalgamated boulder sample (such as 1-meter-protruding boulders from the ridge of Cerro

304   Anay). The x-axis shows the range of modelled boulder denudation rates, and the y-axis shows

305   the range of modelled soil denudation rates. However, not every combination within the range

306   plotted in Fig. 6 is plausible. For example, the part of the colored bands in Fig. 6 that is close to

307   the 1:1-line (edge of the gray area) exists because at very low differential denudation rates

308   (differences between soil and boulder denudation rates), phase 2 gets very long so that the

309   boulder denudation rate dominates the resulting concentration and approaches the value one

310   would obtain when neglecting the first term on the right side in Eq. 1. We argue that differential

311   denudation rates of less than ~1 m Myr^{-1} are highly unlikely, as it would take ~1 Myr to exhume a

312   boulder of only 1 m in height above the soil, while simultaneously eroding many times more soil

313   and boulder material.

314   In NA, permissible modelled soil denudation rates range from ~13 to 37 m Myr^{-1} and

315   permissible modelled boulder denudation rates range from ~5 to 20 m Myr^{-1} (Fig. 6A). Three

316   samples that were taken from the same ridge at Cerro Anay (Fig. 2A3 and 4A) all overlap in

317   denudation rate despite varying protrusion heights. These samples also overlap with a sample

318   from Casa de Piedras, and together indicate a rather narrow range of soil and boulder denudation

319   rates of ~15-20 m Myr^{-1} and ~10-15 m Myr^{-1}, respectively. Only the mid-slope sample from

14

320   Cerro Anay has higher modelled soil and boulder denudation rates. In LC, modelled boulder and

321   soil denudation rates that are consistent with the measured ^{10}Be concentrations extend to much

322   higher values compared to the other field sites (40-140 m Myr^{-1}; Fig. 6B) and the two solutions

323   do not overlap. In SG, permissible modelled denudation rates are similar in magnitude to results

324   from NA (Fig. 6C); soil denudation rates range from ~7 to 28 m Myr^{-1} and boulder denudation

325   rates range from ~4 to 23 m Myr^{-1}. Samples taken from the ridge of Santa Gracia Hill (Fig. 2C2

326   and 4C) have permissible modelled soil and boulder denudation rates that overlap at values of

327   ~12-15 m Myr^{-1} and ~10-12 m Myr^{-1}, respectively, whereas samples from the ridge of Zebra Hill

328   overlap at ~4-5.5 m Myr^{-1} for boulders and ~6.5-7.5 m Myr^{-1} for soil. Samples from the slope of

329   Santa Gracia Hill have higher modelled soil denudation rates, when considering very low

330   differential denudation rates unlikely. We further discuss the most plausible ranges of denudation

331   rates in sections 5.1 and 5.2.

332   **4.3   Fault and stream orientations**

333   Fault orientations in our field sites, based on straight segments of 100 m (8,731 segments

334   for SG, 6,572 segments for LC, and 6,214 segments for NA), generally have at least one

335   dominant orientation that aligns with stream orientations (Fig. 7). Stream orientations depend on

336   the flow accumulation threshold: at smaller thresholds (10^4 m^2), abundant small streams yield a

337   wide distribution of orientations that seems to reflect the shape of the catchment as a whole. At a

338   high flow accumulation threshold (10^6 m^2), the derived stream networks comprise only the largest

339   channels and their orientation is strongly controlled by the orientation and tilt of the drainage

340   basin. This can be seen clearly in NA, where the east-west oriented trunk stream is weighted

341   heavily. In SG, faults and stream orientations match each other well, both trending north-south. In

342   LC and NA, one of two regional fault orientations match stream orientations, and faults closest to

343   the field sites more closely match dominant stream orientations (red faults in Fig. 7). Specifically,

344   in LC, the dominant orientations for the regional faults are roughly northeast and secondarily

345   northwest, whereas streams are generally oriented northwest. In NA, faults generally have east-

346   west and northwest-southeast orientations, and streams with an accumulation threshold above 10^4

347   follow an east-west orientation. Fracture orientations measured in the field (in NA) also generally

348   agree with the larger fault and stream orientations, with mostly west-northwest – east-southeast

349   orientations (Fig. 5B). Our fracture spacing measurements are mostly in the range of 2-15 meters

350   (Fig. 5A), while our boulder width measurements are generally smaller (0-5 meters). When

351   plotted together, the distribution of boulder sizes sits at the left tail of the distribution of the

352   fracture spacing measurements (Fig. 5C).

353   **5   Discussion**

354   **5.1   Deciphering the denudation rates of boulders and soil**

355   Our model results show that there exists no unique combination of soil and boulder

356   denudation rates for any particular site (Fig. 6). Which, then, are the most plausible combinations

357   of boulder and soil denudation rates? The answer depends on the characteristic exhumation

358   histories of the boulders, and events that could have influenced the accumulation of ^{10}Be during

359   the course of exhumation. In order to narrow down the ranges of denudation rates for boulders

360   and soils investigated in this study, we address our model assumptions and complicating factors,

361   such as shielding and toppling of boulders, and compare measured and modelled ^{10}Be

362   concentrations of soils to each other.

363   Our model rests on five main assumptions outlined at the end of section 3.1.3. The first,

364   long-term steady state of the landscape, is difficult to assess; however, the lack of knickpoints

365   above our sampling locations (Fig. S1) suggests this to be reasonable. With our dataset, it is also

366   difficult to assess assumption two, whether soil denudation rates were steady or variable

367   throughout boulder exhumation; however, we speculate on this possibility below. Assumptions 3

368   and 4, regarding boulder mobility and shielding, are discussed in depth in the next section.

369   Assumption 5 is that the density of soil can be treated like the density of boulders and bedrock.

370   Although the density of soil and saprolite layers is in reality lower, we assume a steady thickness

371   of these layers through time, which means that the lowering of the bedrock-saprolite boundary

372   occurs at the same rate as that of the soil surface. The actual thickness of the soil and saprolite

373   layers is relatively unimportant (Granger and Riebe, 2014), and thus one can consider the

374   thickness to be zero. While this approach may appear unrealistic, it is important to note that the

375   attenuation of cosmogenic nuclide production with depth depends on length times density, and a

376   lower density soil layer can simply be viewed as inflated bedrock.

377   **5.1.1   Shielding and toppling of boulders**

378   There exist two scenarios that would lead to violations of our model assumptions 3 and 4,

379   and would inadvertently introduce bias into our approach of determining boulder denudation

380   rates: (1) sampling of boulders that have been previously shielded by soil or other boulders, and

381   (2) sampling of boulders that have toppled or rolled downhill, and that are no longer in situ. In

382   either case, the actual production rate for the sample would be lower than assumed, leading to an

383   artificially high denudation rate estimate. Shielding by boulders is more likely in areas where

384   there are tall, densely-clustered boulders, or at protruding bedrock outcrops such as Piedra de

385   Aguila, where we measured a very low [10]Be concentration in sample NB-BR4 (Table 1; Fig. 4A).

386   This sample was taken from a bedrock knob close to a cliff in an area accessed by tourists; it is

387   possible that the low concentration of our sample is due to shielding by boulders that toppled, or

388   were manually moved from the sampled area.

389   Boulders in steeply sloping areas are more likely to be shielded by soil or topple downhill.

390   In LC, where slopes are generally steeper than the other field sites, it is possible that some

391   boulders were not in situ when we sampled them: they could have rolled or been overturned on

392   the steep slopes, uncovering a side that was previously shielded. They could have also been

393   transiently shielded by soil coming from upslope (Fig. 2B3). In addition, there is a significant

394   relationship between protrusion height and hillslope angle for LC boulders, indicating that

395   boulders on steeper slopes are either smaller, or may be partially buried by upslope soil (Fig. 5E).

396   Indeed, three boulder samples from LC (LC2, LC4, and LC18; Table 1) have measured ^{10}Be

397   concentrations that are lower than the surrounding soil, violating our model assumptions, and

398   suggesting that the sampled boulder surfaces were shielded. Two of these amalgamated boulder

399   samples (LC4 and LC18) were collected from slopes with rather high angles of 27° and 18°,

400   respectively, and therefore could include toppled boulders. Boulder sample LC2 however was

401   collected on a ridge with a relatively lower slope of 9° (Table 1). In that case, the low ^{10}Be

402   concentration could stem from shielding by stacked boulders (scenario 1). In NA, one boulder

403   sample (NA15; Table 1) also has a very low ^{10}Be concentration and was not included in the

404   model. We did not collect a soil sample near the boulder sample NA15, and instead compared its

405   concentration to the adjacent surficial soil pit sample of Schaller et al. (2018). Because these

406   samples were not taken exactly next to each other, there exists some ambiguity in this

407   comparison. However, the relatively low ^{10}Be concentration of sample NA15 when compared to

408   other boulder samples in NA suggests issues that could be related to shielding or toppling of

409   boulders. Over long timescales, we expect all sampled boulders to be fully exhumed and either

410   weather away completely in place or topple down the hill, eventually ending up in streams where

411   they would be exported from the catchment. It is plausible that such a cycle of boulder exposure,

412   exhumation, and transport has operated in the past and will continue into the future. In LC, due to

18

413   higher hillslope angles and overall higher denudation rates, this cycle seems to be occurring at a

414   faster rate, probably leading to a higher chance of sampling boulders that have more recently

415   been exhumed and rolled downhill.

5.1.2   Plausible ranges for modelled denudation rates

417   For most of our soil samples, measured ^{10}Be concentrations agree well with modelled

418   ^{10}Be concentrations (Table 2), suggesting that our model setup and assumptions are reasonable.

419   Positive or negative deviations stemming from soil samples collected in the field are expected,

420   however, because (1) our soil samples are most likely a mixture between lower concentration soil

421   that is directly exhumed from below, and higher concentration grains eroded from the

422   surrounding boulders, (2) soil surrounding boulders could be blocked from moving downslope by

423   the boulders themselves (as shown in Glade et al., 2017), which could slow down soil transport

424   and raise soil ^{10}Be concentrations, (3) we did not account for shielding of soil by the surrounding

425   boulders, which would lower production rates, and (4), quartz could be enriched in weathered

426   soils (Riebe and Granger, 2013). In most cases, the modelled soil concentrations are slightly

427   lower than the measured soil concentrations, which suggests that cases 1, 2, or 4 are common in

428   our field sites. The relevance of case 4 (quartz enrichment) depends on the degree of chemical

429   weathering, and can lead to an overestimation of ^{10}Be concentrations. Work by Schaller and

430   Ehlers (2022) suggests that on average about half the mass loss in La Campana and Santa Gracia

431   occurs by chemical weathering in soil and saprolite, but only about a quarter in Nahuelbuta.

432   However, their data stem from meter-deep soil pits, whereas our soil samples were collected from

433   areas in between boulders, where the soil depth is probably less deep, and also variable. In order

434   to calculate a quartz enrichment factor, we would need additional geochemical data, such as

435   zircon enrichment in soils and bedrock, which we do not have; therefore, we can only assume the

19

436   possibility of some quartz enrichment leading to higher-than-expected ^{10}Be concentrations in our

437   soil samples.

438   In one sampling site (Casa de Piedras in NA), the measured soil ^{10}Be concentration is

439   significantly lower than the modelled soil ^{10}Be concentration (Table 2). If the soil was eroding as

440   fast as our measured soil samples indicate, the boulders should be protruding higher. However,

441   Casa de Piedras has a high density of tall boulders. The observed discrepancy could be caused by

442   boulders shielding the soil directly surrounding it from cosmic rays, or by eroding chips with low

443   ^{10}Be concentrations of shielded parts of the boulders, perhaps from the base, that fall directly into

444   the soil.

445   Another discrepancy exists in the relationship between measured ^{10}Be concentrations and

446   protrusion heights of our sampled boulders. No significant relationship exists between protrusion

447   height and ^{10}Be concentration for all samples plotted together (Fig. 5D); this is to be expected as

448   each individual site has a unique local denudation rate. On the other hand, one would expect a

449   relationship between protrusion and concentration for boulders sampled from the same site (i.e. at

450   Cerro Anay ridge in NA, and Santa Gracia Hill and Zebra Hill in SG). At Santa Gracia Hill and

451   Zebra Hill, taller boulders have a higher ^{10}Be concentration, as expected, but the highest-

452   protruding boulder sample from Cerro Anay has a lower concentration than the second-tallest

453   sample, perhaps due to toppling of pieces of the tallest boulders. The differential erosion rate

454   between boulders and soil at Cerro Anay ridge is also one of the highest for NA at 5 m Myr^{-1}

455   (Table 2), indicating relatively rapid exposure of boulders that may raise the risk of boulder

456   toppling. However, there is an overlap in the modelled denudation rates of all three boulder and

457   soil sample pairs from Cerro Anay ridge (Fig. 6A).

458   The lack of a trend between boulder protrusion height and ^{10}Be concentration could also

459   be due to changing soil denudation rates over time. Taller boulders and boulders with longer

20

460   residence times (such as those on the slope of Cerro Anay Hill in NA and the slope of Santa

461   Gracia Hill in SG; Table 2), were exhumed during one or more glacial-interglacial cycles; during

462   such climatic transitions, soil denudation rates could have changed. Similarly, Raab et al. (2019)

463   suggested that soil denudation rates surrounding tors in southern Italy shifted in conjunction with

464   climate changes over the course of their exhumation (around 100 ka). However, our approach

465   yields an average soil denudation rate over the time of boulder exhumation; therefore, we can

466   only speculate whether soil denudation rates were variable. Carretier et al. (2018) analyzed

467   denudation rate data for Chile averaged over decadal and millennial timescales, and found that

468   millennial denudation rates are higher than decadal erosion rates, with the highest discrepancy

469   between integration time periods being in the arid north. However, the authors suggest that this

470   discrepancy is related to increased stochasticity of erosion in arid regions; millennial erosion rates

471   reflect many stochastically erosive events, such as 100-year floods, that decadal rates do not

472   record.

473   Given the above caveats and uncertainties, we attempted to identify the most plausible

474   range of denudation rates for each sample type and location for all modelled denudation rates.

475   Specifically, we identified most plausible denudation rate ranges for samples on Cerro Anay

476   ridge and Casa de Piedras based on their overlap with each other, for samples on Cerro Anay

477   slope based on their overlap with sample NA9 on Cerro Anay ridge, and ranges for Santa Gracia

478   hill ridge and slope and Zebra Hill ridge based on the overlap of modelled rates for each location,

479   respectively (Fig. 6). For LC we regard denudation rates near the center of the modelled curves in

480   Figure 5 to be most plausible, based on reasonable expectations of differential erosion (section

481   4.2), and considering possible issues with shielding and toppling (section 5.1). These ranges are

482   listed in Table 2 along with measured and modelled ^{10}Be concentrations of soil samples, and are

483   displayed in Fig. 8 along with previously published soil (Schaller et al., 2018) and catchment-

484   average denudation rates (van Dongen et al., 2019). In the following section, we discuss the

485   erosional processes that may account for the differences and similarities in denudation rates from

486   bedrock, boulders, soil (this study and Schaller et al., 2018), and stream sediment (van Dongen et

487   al., 2019) within each field site. We focus on the modelled denudation rates from this study that

488   we regard to be most plausible.

489   **5.2   Processes controlling differential erosion**

490   **5.2.1   Nahuelbuta (NA)**

491   In NA, the slowest denudation rates occur on bedrock and boulders, likely because

492   precipitation runs off quickly from exposed bedrock, limiting its chemical alteration (Eppes and

493   Keanini, 2017) and weathering (Hayes et al., 2020), whereas soils denude faster. However,

494   denudation rates for soil surrounding the sampled boulders are lower than denudation rates from

495   the soil pit and the catchment average denudation rates. It is possible that boulders physically

496   block soil from being transported downslope: where a dense clustering of exhumed boulders

497   exists, the regolith will be thinner, and the boulders may retard soil erosion throughout the area in

498   which they are clustered (Glade et al, 2017). Considering boulder protrusion and modelled

499   differential erosion rates, boulders in NA are exposed over a long period (up to 640 Kyr),

500   allowing time to affect the long-term transportation of surrounding soil downslope. Although we

501   did not measure sediment damming upslope of boulders in the field, we did note a small amount

502   of sediment damming for boulders on slopes. Away from exhumed boulders, where soil is thicker

503   and where slopes are steep enough, shallow landsliding can occur, as observed in NA by Terweh

504   et al. (2021). In accordance with these observations, van Dongen et al. (2019) found that smaller

505   grains in stream sediment were likely derived from the upper mixed soil layer, and the largest

506   grains were likely excavated from depth, perhaps by shallow landsliding. The smaller grains have

507   denudation rates similar to those presented in this study (Fig. 8), while larger grains have

508   denudation rates similar to deeper soil pit samples from Schaller et al. (2018).

509   Finally, in NA, where bedrock fracture density is higher, denudation rates are also higher

510   (Fig. 8), likely because precipitation infiltrates into fractures, accelerating chemical weathering,

511   regolith formation (St. Claire et al., 2015; Lebedeva and Brantley, 2017), and subsequent

512   vegetation growth, which introduces biotic acids that further accelerate chemical weathering

513   (Amundson et al., 2007). We further speculate that large exhumed boulders in NA are also sites

514   of less-fractured bedrock at depth, as boulders can only be as large as the local fracture spacing

515   allows (e.g. Sklar et al., 2017). Based on the observed differences in soil, boulder, and fractured

516   bedrock denudation rates in NA, and on previous studies that have correlated higher fracture

517   density with more rapid erosion (e.g., Dühnforth et al., 2010; DiBiase et al., 2018; Neely et al.,

518   2019), we suggest that bedrock fractures have an effect on NA's morphology through grain size

519   reduction and differential erosion. Further, the thicker soil cover and shallow landsliding on NA

520   slopes may increase the discrepancy between slowly-eroding bedrock and boulders versus more

521   rapidly-eroding, vegetation-covered hillslopes, eventually causing bedrock and boulders to sit at

522   topographic highs, as we observed in the field.

523   **5.2.2 La Campana (LC)**

524   In LC we observe the largest range of denudation rates between bedrock, boulders, soil,

525   and stream sediment, and also the highest overall denudation rates of the three field sites. We

526   suspect that both of these characteristics are related to slope angles, which are on average nearly

527   twice as steep as in NA and SG (Table 1; van Dongen et al., 2019). It should be noted that the

528   stream sediment samples were taken from an adjacent catchment that does not drain the hillslopes

529   sampled in this study, and the generally low and wide-ranging [10]Be concentrations in the stream

530 sediment have been related to relatively recent landslides observed in the upper headwaters (van

531 Dongen et al., 2019; Terweh et al., 2021). However, steep slopes are pervasive throughout LC

532 and lead us to suggest that shallow landslides are important erosional processes in this field site.

533   In LC we frequently observed boulder samples with lower ^{10}Be concentrations than

534 adjacent soil samples (Table 1, section 5.1), which is inconsistent with our simple model of

535 boulder exhumation (Fig. 3), and is possibly because the sampled boulders were not exhumed in

536 situ (section 5.1.1). Landslides as observed in LC can bring down boulders in the processes of

537 downhill movement, and may cause the excavation of larger blocks from greater depth before

538 their size is reduced in the weathering zone. More vigorous mass wasting is consistent with larger

539 average hillslope grain sizes for LC, as compared to NA and SG (Terweh et al., 2021). In general,

540 the high relief, steep slopes, and high denudation rates suggest that tectonic uplift rates in LC

541 could be higher than assumed for the nearby coast (Melnick, 2016). Modelled differential

542 denudation rates between boulders and soil are the highest of all field sites, and therefore the time

543 needed to reach the measured boulder protrusion heights is the lowest (23 and 7 Kyr; Table 2),

544 suggesting relatively rapid turnover of boulder exposure and movement downslope. However, we

545 did note some sediment damming by boulders on LC slopes (Fig. 2B3), and in all cases in LC the

546 modelled soil denudation rates are lower than measured soil denudation rates, suggesting that

547 boulders are locally suppressing soil denudation to some extent on LC slopes.

548   Finally, although the role that fracturing plays in LC is difficult to assess, note that our

549 bedrock sample has a significantly lower denudation rate than boulders and soils (Fig. 8), despite

550 being on a steep slope (Table 1). Rolling and toppling processes that may be relevant for LC

551 boulders are not plausible for the bedrock patch, allowing its nuclide concentration to be high.

552 Likewise, the boulder denudation rate from the ridge sample LC1, where the risk of toppling is

553 likely the lowest, is similar to the bedrock denudation rate. Additionally, LC's mediterranean

24

climate features frequent fires, which cause spalling of rock flakes off boulder surfaces. While

LC boulders are surrounded by shrubs that occasionally burn, causing spalling of boulder

surfaces, the extensive bedrock patch in LC is free of vegetation and therefore at a lower risk for

fire-induced erosion.

5.2.3   Santa Gracia (SG)

In the semi-arid landscape of SG, as in humid-temperate NA, boulders are eroding more

slowly than the surrounding soil, but the differences in boulder and soil denudation rates are

subtle. This leads to a slow exposure of hillslope boulders, with exposure of current boulder

protrusion (based on differential modelled denudation rates) taking up to 870 Kyr (Table 2). In

addition, denudation rate differences between ridge and slope samples – possibly related to slope

angle – are larger than the differences between boulders and soil. Furthermore, unlike in NA, our

boulder and soil denudation rates are within the same range as the soil pit and catchment average

denudation rates (Fig. 8), suggesting that erosional efficiencies are similar across different

sediment sizes. Van Dongen et al. (2019) also measured relatively constant catchment average

[10]Be concentrations over seven grain size classes in SG (Fig. 8), which suggests that all grain

sizes have been transported from the upper mixed layer of hillslope soil and that deep-seated

erosion processes are unlikely, in accordance with absent landsliding (Terweh et al., 2021). Thus,

our results agree with previous findings that erosion in SG is likely limited to grain-by grain

exfoliation of boulders and the slow diffusive creep of the relatively thin soil cover on hillslopes

(Schaller et al., 2018). When bedrock is exhumed, its long residence time on hillslopes allows it

to weather slowly in place and reduce in size, with minimal transportation of weathered material

by runoff and a low degree of chemical weathering and soil production (Schaller and Ehlers,

2022).

577   Such a narrow range of relatively low denudation rates indicates that very long time

578   periods are necessary to produce relief between hilltops and valleys. Note, however, despite low

579   uplift rates in SG, the total mean basin slope in SG is 17° compared to 9° in NA (van Dongen et

580   al., 2019). This could be due to low MAP resulting in a low erosional efficiency in SG, which, in

581   order to achieve denudation rates that match uplift rates, requires the slopes to be steeper

582   (Carretier et al., 2018). Although the differences in denudation rates between grain sizes is subtle

583   in SG, soils have higher denudation rates than the boulders they directly surround. Additionally,

584   the measured denudation rates of soil surrounding boulders on SG slopes are lower than modeled

585   soil denudation rates (Table 2), indicating that boulders may be prolonging the residence time of

586   the surrounding soil by a small amount, either by blocking its movement downslope or by

587   contributing grains through exfoliation.

588   **5.3   Fracture control on larger-scale landscape evolution**

589   We have shown that, in our field sites, bedrock denudes the slowest, followed by

590   boulders, and finally soil. In each climate zone, and especially where chemical weathering plays a

591   large role (NA), sediment size is likely controlled by the spacing of bedrock fractures. Once on

592   the surface, on low or moderate slopes, large boulders initially delineated by fracture spacing are

593   more difficult to transport than smaller sediment, and therefore locally retard denudation rates.

594   On the landscape scale, such differential erosion should lead to landscape morphologies

595   controlled by fracture spacing patterns. In NA, we were able to measure fracture density in

596   several bedrock outcrops and found that average higher fracture density is correlated with higher

597   denudation rates (Fig. 5A). It is plausible that the measured fracture spacing in bedrock outcrops

598   represents the parts of the landscape where bedrock fracture density is the lowest, and it is highest

599   under the soil mantled parts of the landscapes, where fractures are not exposed. Fracture spacing

600   in NA is generally larger than boulder width (Fig. 5C), although there is overlap. If we assume

601   that boulder width is initially delineated by fracture spacing at depth, our results indicate that

602   boulders have reduced in size in the weathering zone prior to and during exhumation. If we

603   further assume that hillslope sediment lies on a spectrum with unweathered blocks delineated by

604   fractures on one end, and sediment that has been significantly reduced in size in the weathering

605   zone on the other end (e.g. Verdian et al., 2021), boulders in NA seem to fall somewhere in the

606   middle.

607   Bedrock fracture patterns also likely affect stream incision in a similar way, by dissecting

608   bedrock and reducing sediment size, making it easier to be transported by flowing water. This

609   phenomenon may be visible in our field sites on a larger scale, through the similarity of fault and

610   stream orientations. In NA, our fracture orientation measurements (Fig. 5B) are similar to fault

611   and stream orientations (Fig. 7). In general, as tectonically-induced faults and fractures are

612   products of the same regional stresses, we assume that regional faults have orientations consistent

613   with fractures in our field sites (c.f., Krone et al., 2021). Regional faults and smaller fractures

614   have been shown to be closely related: Rodriguez Padilla et al. (2022) mapped fractures resulting

615   from the 2019 Ridgecrest earthquakes in bedrock and sediment-covered areas, and found that

616   fracture density decreases from main faults with a power law distribution. They also found that

617   the orientations of faults and fractures were closely matching. Fracture orientation has also been

618   shown to influence stream orientation. Roy et al. (2015) modeled stream incision in a landscape

619   dissected by dipping weak zones, meant to resemble fracture or fault zones, and found that in

620   cases with a large contrast in bedrock weakness (>30x), channels migrated laterally to follow the

621   shifting exhumation of the weak zone. In our field sites, we observe that stream channels ($A_{min} \geq$

622    $10^5 \, m^2$) generally follow fault orientations (Fig. 7). This is especially clear in SG, where the

623   north-south striking Atacama Fault System is reflected in the orientation of faults, streams, and

624   also fractures measured in a nearby drill core (Krone et al., 2021; Fig. 7). In LC and NA, despite

625   more variety in fault and stream orientations, streams closest to the field sites tend to align with

626   fault orientations (Fig. 7). Especially in NA, the larger streams are often nearly perpendicular to

627   each other, similar to rectangular drainage networks, which are often indicative of structural

628   control on drainage patterns (e.g., Zernitz, 1932). These results suggest that within the same rock

629   type, local fracture patterns induced by regional faults can induce differential denudation in

630   landscapes.

631   In summary, we argue that in NA, and possibly also in SG and LC, bedrock fracturing

632   influences landscape morphology by setting grain size and thus dictating patterns of denudation

633   rates on hillslopes and in streams: in situ hillslope boulders likely originated as blocks set by

634   fracture spacing, and after being exhumed, locally suppress denudation as described above. This

635   interpretation is supported by work in Puerto Rico; Buss et al. (2013) studied corestones from two

636   boreholes cutting through regolith in the Luquillo Experimental Forest, and found that corestones

637   decreased in size with increased chemical weathering and exhumation through the regolith

638   profile. They deduced that the corestones likely started as bedrock blocks delineated by fractures.

639   Further, they found that the borehole drilled near a stream channel contained more highly-

640   fractured bedrock compared to the borehole drilled at a ridge, and inferred that corestone size was

641   larger under the ridge due to lower bedrock fracture density. In accordance with Fletcher and

642   Brantley (2010), they concluded that, if erosion and weathering increase with bedrock fracture

643   density, then the ridges and valleys in their study area could be controlled by fracture density

644   patterns.

645   We therefore offer the following conceptual model: in a landscape with fractured bedrock

646   (Fig. 9A), areas with higher fracture density should be sites of smaller hillslope sediment sizes

647   (e.g. Sklar et al., 2017; Neely and DiBiase, 2020), where rainfall can easily infiltrate, conversion

648   of bedrock to regolith is easiest (St. Claire et al., 2015; Lebedeva and Brantley, 2017), and

649   denudation rates are highest. Over time, precipitation will divergently run off topographic highs

650   and starve bedrock and larger boulders on high points while infiltrating into topographic lows,

651   where streams eventually incise (Bierman, 1994; Hayes et al., 2020; Fig. 9B). Bedrock and

652   boulders on topographic highs denude more slowly than finer sediment and soil, accentuating any

653   elevation differences. Regolith also promotes vegetation growth, which slows runoff, raises rates

654   of infiltration, and enhances chemical weathering (Amundson et al., 2007; Fig. 9B). In steeper

655   landscapes, such as LC, boulders will be more mobile and may roll down the hillslopes,

656   eventually ending up in stream channels where they may shield the channel bed from denudation

657   (DiBiase et al., 2017; Shobe et al., 2016; Fig. 9C). In addition, in such higher relief landscapes,

658   fractures due to topographic stresses from exhumation may form at topographic highs as the

659   topography emerges (St. Claire et al., 2015), countering this positive feedback loop (Fig. 9C).

660   Over longer timescales, bedrock with different patterns of fracture density may be exhumed,

661   which can invert landscapes to reflect the new fracture patterns exposed at the surface (Roy et al.,

662   2016). In this way, fracturing, climate, and residence time can operate in conjunction to set the

663   sediment size and morphology of hillslopes and streams within landscapes.

664   **6   Conclusions**

665   In this study, we explored the ability of bedrock patches and large boulders to retard

666   denudation and influence landscape morphology, in three relatively slowly-eroding landscapes

667   along a climate gradient in the Chilean Coastal Cordillera. Based on *in situ* cosmogenic [10]Be-

668   derived denudation rates of bedrock, boulders and soil, we find that in almost all cases across the

669   three sites studied, soil denudation rates are by ~10-50% higher than the denudation rates of the

670   boulders that they surround, which are more similar to bedrock denudation rates. This pattern is

671 more complicated in La Campana, where some boulders have lower [10]Be concentrations than the

672 surrounding soil, perhaps because they were overturned or covered with soil at some point due to

673 steeper slopes. These results suggest that exposed bedrock patches and large hillslope boulders

674 affect landscape morphology by slowing denudation rates, eventually forming the nucleus for

675 topographic highs. On the other hand, our work also suggests that where slopes are close to the

676 angle of repose and where landsliding is observed (as in La Campana), while bedrock patches

677 denude slowly and likely retard hillslope denudation, hillslope boulders may have a smaller or

678 even negligible effect on suppressing denudation.

679   In addition, we found that bedrock fracturing and faulting accelerates hillslope denudation

680 and stream incision in our field sites: hillslope denudation rates increase with fracture density in

681 NA, and streams tend to follow the orientation of larger faults in all three sites. We infer that

682 bedrock fracture patterns in our field sites set grain sizes on hillslopes, and bedrock patches and

683 boulders represent locations where fracture density is lower, and thus weathering, erosion, and

684 soil formation are suppressed. On a larger scale, our results imply that tectonic preconditioning

685 in the form of bedrock faulting and fracturing influences landscape evolution by impacting the

686 pathway of streams, as well as the migration of ridges, as landscapes denude through layers of

687 bedrock preconditioned by tectonic fracturing over time, and encounter varying levels of

688 resistance depending on the fracture density.

689 **7   Acknowledgements**

694   the Chilean National Park Service (CONAF) for providing access to the sample locations and on-

695   site support of our research. We also thank Iris Eder and David Scheer for their help in the field

696   and in the laboratory, Cathrin Schulz for her help in the laboratory, and Steven A. Binnie and

697   Stefan Heinze from Cologne University for conducting AMS measurements.

698   **8   Data Availability**

699   Cosmogenic nuclide data and Matlab-scripts of the model presented in this paper will be

700   made available as a GFZ Data Publication in accordance with FAIR principles. LiDAR data from

701   the studied catchments is available in Krüger et al. (2022).

702   **9   References**

703   Amundson, R., Richter, D. D., Humphreys, G. S., Jobbágy, E. G., and Gaillardet, J.: Coupling

704   between biota and earth materials in the critical zone, Elements, 3 (5), 327-333,

705   https://doi.org/10.2113/gselements.3.5.327, 2007.

706   Alaska Satellite Facility Distributed Active Archive Center: ALOS

707   PALSAR_Radiometric_Terrain_Corrected_high_res (ALPSRP191976520), includes Material ©

708   JAXA/METI 2009, ASF DAAC [dataset], https://doi.org/10.5067/Z97HFCNKR6VA, 2009.

709   Alaska Satellite Facility Distributed Active Archive Center: ALOS

710   PALSAR_Radiometric_Terrain_Corrected_high_res (ALPSRP269644390), includes Material ©

711   JAXA/METI 2011, ASF DAAC [dataset], https://doi.org/10.5067/Z97HFCNKR6VA, 2011.

712   Alaska Satellite Facility Distributed Active Archive Center: ALOS

713   PALSAR_Radiometric_Terrain_Corrected_high_res (ALPSRP277746590), includes Material ©

714   JAXA/METI 2011, ASF DAAC [dataset], https://doi.org/10.5067/Z97HFCNKR6VA, 2011.

715   Attal, M., Mudd, S. M., Hurst, M. D., Weinman, B., Yoo, K., and Naylor, M.: Impact of change

716   in erosion rate and landscape steepness on hillslope and fluvial sediments grain size in the Feather

717   River basin (Sierra Nevada, California), Earth Surf. Dynam., 3, 201–222.

718   https://doi.org/10.5194/esurf-3-201-2015, 2015.

719   Balco, G., Stone, J. O., Lifton, N. A., and Dunai, T. J.: A complete and easily accessible means of

720   calculating surface exposure ages or erosion rates from 10Be and 26Al measurements, Quat.

721   Geochronol., 3, 174–195, https://doi.org/10.1016/j.quageo.2007.12.001, 2008.

722   Balco, G., Purvance, M.D. and Rood, D.H.: Exposure dating of precariously balanced rocks,

723   Quat. Geochronol., 6(3-4), 295-303, https://doi.org/10.1016/j.quageo.2011.03.007, 2011.

724   Bierman, P.: Using in situ produced cosmogenic isotopes to estimate rates of Landscape

725   evolution: A review from the geomorphic perspective, J. Geophys. Res.: Solid Earth, 99 (B7),

726   13885-13896, https://doi.org/10.1029/94JB00459, 1994.

727   Bierman, P. R. and Caffee, M. W.: Cosmogenic exposure and erosion history of Australian rock

728   landforms, Geol. Soc. of America Bulletin., 114, 787–803, https://doi.org/10.1130/0016-

729   7606(2002)114<0787:CEAEHO>2.0.CO;2, 2002.Boisier, J. P., Alvarez-Garretón, C., Cepeda, J.,

730   Osses, A., Vásquez, N., and Rondanelli, R.: CR2MET: A high-resolution precipitation and

731   temperature dataset for hydroclimatic research in Chile, EGU General Assembly 2018, April

732   2018, EGU2018-19739, 2018.

733   Borchers, B., Marrero, S., Balco, G., Caffee, M., Goehring, B., Lifton, N., Nishiizumi, K.,

734   Phillips, F., Schaefer, J., and Stone, J.: Geological calibration of spallation production rates in the

735   CRONUS-Earth project, Quat. Geochronol., 31, 188-198,

736   https://doi.org/10.1016/j.quageo.2015.01.009, 2016.

737   Braucher, R., Merchel, S., Borgomano, J., and Bourlès, D.L.: Production of cosmogenic

738   radionuclides at great depth: A multi element approach, Earth Planet. Sc. Lett., 309, (1–2), 1-9,

739   https://doi.org/10.1016/j.epsl.2011.06.036, 2011.

740   Burbank, D. W., Leland, J., Fielding, E., Anderson, R. S., Brozovic, N., Reid, M. R., and Duncan,

741   C.: Bedrock incision, rock uplift and threshold hillslopes in the northwestern Himalayas, Nature,

742   379, 505–510, https://doi.org/10.1038/379505a0, 1996.

743   Buss, H.L., Brantley, S.L., Scatena, F.N., Bazilievskaya, E.A., Blum, A., Schulz, M., Jiménez, R.,

744   White, A.F., Rother, G. and Cole, D.: Probing the deep critical zone beneath the Luquillo

745   Experimental Forest, Puerto Rico, Earth Surf. Proc. Land., 38(10), 1170-1186,

746   https://doi.org/10.1002/esp.3409, 2013.

747   Callahan, R.P., Riebe, C.S., Pasquet, S., Ferrier, K.L., Grana, D., Sklar, L.S., Taylor, N.J.,

748   Flinchum, B.A., Hayes, J.L., Carr, B.J. and Hartsough, P.C.: Subsurface weathering revealed in

749   hillslope-integrated porosity distributions, Geophys. Res. Lett., 47(15),

750   https://doi.org/10.1029/2020GL088322, 2020.

751   Carretier, S., Tolorza, V., Regard, V., Aguilar, G., Bermúdez, M.A., Martinod, J., Guyot, J-L,

752   Hérail, G., and Riquelme, R.: Review of erosion dynamics along the major N-S climatic gradient

753   in Chile and perspectives, Geomorphology, 300, 45-68,

754   https://doi.org/10.1016/j.geomorph.2017.10.016, 2018.

755   Chilton, K.D. and Spotila, J.A.: Preservation of Valley and Ridge topography via delivery of

756   resistant, ridge-sourced boulders to hillslopes and channels, Southern Appalachian Mountains,

757   USA, Geomorphology, 365, 107263, https://doi.org/10.1016/j.geomorph.2020.107263, 2020.

758   Clair, J. St., Moon, S., Holbrook, W.S., Perron, J.T., Riebe, C.S., and Martel, S.J.: Geophysical

759   imaging reveals topographic stress control of bedrock weathering, Geomorphology, 350 (6260),

760   https://doi.org/10.1126/science.aab2210, 2015.

761   Coira, B., Davidson, J., Mpodozis, C., and Ramos, V.: Tectonic and Magmatic Evolution of the

762   Andes of Northern Argentina and Chile, Earth Sci Rev., 18, 303-332,

763   https://doi.org/10.1016/0012-8252(82)90042-3, 1982.

764   Dewald, A., Heinze, S., Jolie, J., Zilges, A., Dunai, T., Rethemeyer, J., Melles, M., Staubwasser,

765   M., Kuczewski, B., Richter, J., Radtke, U., von Blanckenburg, F., and Klein, M.: Cologne AMS,

766   a dedicated center for accelerator mass spectrometry in Germany, Nucl. Instrum. Meth., B 294,

767   18-23, dx.doi.org/10.1016/j.nimb.2012.04.030, 2013.

768   DiBiase, R. A., Lamb, M. P., Ganti, V., and Booth, A. M.: Slope, grain size, and roughness

769   controls on dry sediment transport and storage on steep hillslopes, J. Geophys. Res.: Earth Surf.,

770   122, 941–960, https://doi.org/10.1002/2016JF003970, 2017.

771   DiBiase, R. A., Rossi, M. W., and Neely, A. B.: Fracture density and grain size controls on the

772   relief structure of bedrock landscapes, Geology, 46 (5), 399–402,

773   https://doi.org/10.1130/G40006.1, 2018.

774 Dietrich, W.E., Bellugi, D.G., Sklar, L.S., Stock, J.D., Heimsath, A.M., and Roering, J.J.:

775 Geomorphic transport laws for predicting landscape form and dynamics, Geophys. Monogr. -

776 American Geophysical Union, 135, 103-132, https://doi.org/10.1029/135GM09, 2003.

777 Dühnforth, M., Anderson, R.S., Ward, D., and Stock, G.M.: Bedrock fracture control of glacial

778 erosion processes and rates, Geology, 38 (5), 423-426, https://doi.org/10.1130/G30576.1, 2010.

779 Eppes, M. C., and Keanini, R..: Mechanical weathering and rock erosion by climate-dependent

780 subcritical cracking, Rev. Geophys., 55 (2), 470-508, https://doi.org/10.1002/2017RG000557,

781 2017.

782 Fletcher, R.C. and Brantley, S.L.: Reduction of bedrock blocks as corestones in the weathering

783 profile: Observations and model, Am. J. Sci., 310(3), 131-164,

784 https://doi.org/10.2475/03.2010.01, 2010.

785 Glade, R. C., Anderson, R. S., and Tucker, G. E.: Block-controlled hillslope form and persistence

786 of topography in rocky landscape, Geology, 45 (4), 311–314, https://doi.org/10.1130/G38665.1,

787 2017.

788 Glodny, J., Graaefe, K., and Rosenau, M.: Mesozoic to Quaternary continental margin dynamics

789 in South-Central Chile (36–42∘ S): the apatite and zircon fission track perspective, Int. J. Earth

790 Sci., 97, 1271–1291, https://doi.org/10.1007/s00531-007-0203-1, 2008.

791 Granger, D. E., Riebe, C. S., Kirchner, J. W., and Finkel, R. C.: Modulation of erosion on steep

792 granitic slopes by boulder armoring, as revealed by cosmogenic 26Al and 10Be, Earth Planet. Sc.

793 Lett., 186, 269-281, https://doi.org/10.1016/S0012-821X(01)00236-9, 2001.

794   Granger, D. E. and Riebe, C. S.: Cosmogenic Nuclides in Weathering and Erosion, in: Treatise on

795   Geochemistry, Second Edition, edited by: Holland, H. D. and Turekian, K. K., Elsevier, Oxford,

796   7, 401-436, https://doi.org/10.1016/B978-0-08-095975-7.00514-3, 2014.

797   Hayes, N. R., Buss, H. L., Moore, O. W., Krám, P., and Pancost, R. D.: Controls on granitic

798   weathering fronts in contrasting climates, Chem. Geol., 535, 119450,

799   https://doi.org/10.1016/j.chemgeo.2019.119450, 2020.

800   Heimsath, A. M., Chappell, J., Dietrich, W.E., Nishiizumi, K. and Finkel, R.C.: Soil production

801   on a retreating escarpment in southeastern Australia, Geology, 28(9), 787-790,

802   https://doi.org/10.1130/0091-7613(2000)28<787:SPOARE>2.0.CO;2, 2000.

803   Heimsath, A. M., Chappell, J., Dietrich, W. E., Nishiizumid, K., and Finkel, R. C.: Late

804   Quaternary erosion in southeastern Australia: a field example using cosmogenic nuclides, Quat.

805   Internat., 83, 169-185, https://doi.org/10.1016/S1040-6182(01)00038-6, 2001.Kirby, E. and

806   Whipple, K.X.: Expression of active tectonics in erosional landscapes, J. Struct. Geol., 44, 54-75,

807   https://doi.org/10.1016/j.jsg.2012.07.009, 2012.

808   Krone, L.V., Hampl, F.J., Schwerdhelm, C., Bryce, C., Ganzert, L., Kitte, A., Übernickel, K.,

809   Dielforder, A., Aldaz, S., and Oses-Pedraza, R. Perez, J.P.H.: Deep weathering in the semi-arid

810   Coastal Cordillera, Chile, Sci. Rep., 11(1), 1-15, 2021.

811   Kügler, M., Hoffmann, T. O., Beer, A. R., Übernickel, K., Ehlers, T. A., Scherler, D., and Eichel,

812   J.: (LiDAR) 3D Point Clouds and Topographic Data from the Chilean Coastal Cordillera, V. 1.0,

813   GFZ Data Services, https://doi.org/10.5880/fidgeo.2022.002, 2022.

814   Lal, D.: Cosmic ray labeling of erosion surfaces: in situ nuclide production rates and erosion

815   models, Earth Planet. Sc. Lett., 104, 424–439, https://doi.org/10.1016/0012-821X(91)90220-C,

816   1991.

817   Lamb, M. P., Finnegan, N. J., Scheingross, J. S. and Sklar, L. S.: New insights into the mechanics

818   of fluvial bedrock erosion through flume experiments and theory, Geomorphology, 244, 33-55,

819   https://doi.org/10.1016/j.geomorph.2015.03.003, 2015.

820   Lebedeva, M. I. and Brantley, S. L.: Weathering and erosion of fractured bedrock systems, Earth

821   Surf. Proc. Land., 42, 2090–2108, https://doi.org/10.1002/esp.4177, 2017.

822   Martel, S.J.: Mechanics of curved surfaces, with application to surface-parallel cracks, Geophys.

823   Res. Lett., 38(20), https://doi.org/10.1029/2011GL049354, 2011.

824   Melnick, D.: Rise of the central Andean coast by earthquakes straddling the Moho, Nat. Geosci.,

825   9, 1–8, https://doi.org/10.1038/ngeo2683, 2016.

826   Molnar, P., Anderson, R.S., and Anderson, S.P.: Tectonics, fracturing of rock, and erosion, J.

827   Geophys. Res., 112, F03014, https://doi.org/10.1029/2005JF000433, 2007.

828   Mutz, S.G. and Ehlers, T.A.: Detection and explanation of spatiotemporal patterns in Late

829   Cenozoic palaeoclimate change relevant to Earth surface processes, Earth Surf. Dynam., 7(3),

830   663-679, https://doi.org/10.5194/esurf-7-663-2019, 2019.

831   Neely, A.B., DiBiase, R.A., Corbett, L.B., Bierman, P.R., and Caffee, M.W.: Bedrock fracture

832   density controls on hillslope erodibility in steep, rocky landscapes with patchy soil cover,

southern California, USA, Earth Planet. Sc. Lett., 522, 186-197,

https://doi.org/10.1016/j.epsl.2019.06.011, 2019.

Neely, A.B. and DiBiase, R.A.: Drainage Area, Bedrock Fracture Spacing, and Weathering

Controls on Landscape-Scale Patterns in Surface Sediment Grain Size, J. Geophys. Res. Earth

Surf., 125, (10), https://doi.org/10.1029/2020JF005560, 2020.

Oberlander, T. M.: Morphogenesis of Granitic Boulder Slopes in the Mojave Desert, California,

J. Geol., 80, 1–20, https://doi.org/10.1086/627710, 1972.

Oeser, R. A., Stroncik, N., Moskwa, L., Bernhard, N., Schaller, M., Canessa, R., Brink, L. Van

Den, Köster, M., Brucker, E., Stock, S., Pablo, J., Godoy, R., Javier, F., Oses, R., Osses, P.,

Paulino, L., Seguel, O., Bader, M. Y., Boy, J., Dippold, M. A., Ehlers, T. A., Kühn, P.,

Kuzyakov, Y., Leinweber, P., Scholten, T., Spielvogel, S., Spohn, M., Übernickel, K., Tielbörger,

K., Wagner, D., and von Blanckenburg, F.: Chemistry and microbiology of the Critical Zone

along a steep climate and vegetation gradient in the Chilean Coastal Cordillera, Catena, 170, 183–

203, https://doi.org/10.1016/j.catena.2018.06.002, 2018.

Perron, J.T.: Numerical methods for nonlinear hillslope transport laws, J. Geophys. Res. Earth

Surf., 116 (F2), https://doi.org/10.1029/2010JF001801, 2011.

Portenga, E.W. and Bierman, P.R.: Understanding earth's eroding surface with 10Be, GSA

Today, 21, 4–10, https://doi.org/10.1130/G111A.1, 2011.

Raab, G., Egli, M., Norton, K., Dahms, D., Brandová, D., Christl, M. and Scarciglia, F.: Climate

and relief-induced controls on the temporal variability of denudation rates in a granitic upland,

Earth Surf. Proc. Land., 44(13), 2570-2586, https://doi.org/10.1002/esp.4681, 2019.

854 Riebe, C.S. and Granger, D.E.: Quantifying effects of deep and near-surface chemical erosion on

855 cosmogenic nuclides in soils, saprolite, and sediment, Earth Surf. Proc. Land., 38(5), 523-533,

856 https://doi.org/10.1002/esp.3339, 2013.

857 Roda-Boluda, D.C., D'Arcy, M., McDonald, J., and Whittaker, A.C.: Lithological controls on

858 hillslope sediment supply: insights from landslide activity and grain size distributions, Earth Surf.

859 Proc. Land., 43, 956–977, https://doi.org/10.1002/esp.4281, 2018.

860 Rodriguez Padilla, A.M., Oskin, M.E., Milliner, C.W. and Plesch, A.: Accrual of widespread rock

861 damage from the 2019 Ridgecrest earthquakes, Nat. Geosci., 15(3), 222-226, 2022.

862 Roy, S.G., Tucker, G.E., Koons, P.O., Smith, S.M., Upton, P.: A fault runs through it: Modeling

863 the influence of rock strength and grain-size distribution in a fault-damaged landscape, J.

864 Geophys. Res. Earth Surf., 121, https://doi.org/10.1002/2015JF003662, 2016.

865 Roy, S.G., Koons, P.O., Upton, P. and Tucker, G.E.: The influence of crustal strength fields on

866 the patterns and rates of fluvial incision, J. Geophys. Res, Earth Surf., 120(2), 275-299,

867 https://doi.org/10.1002/2014JF003281, 2015.

868 Schaller, M., Ehlers, T.A., Lang, K.A.H., Schmid, M., and Fuentes-Espoz, J.P.: Addressing the

869 contribution of climate and vegetation cover on hillslope denudation, Chilean Coastal Cordillera

870 (26∘–38∘S), Earth Planet. Sc. Lett., 489, 111–122, https://doi.org/10.1016/j.epsl.2018.02.026,

871 2018.

872 Schaller, M. and Ehlers, T.A.: Comparison of soil production, chemical weathering, and physical

873 erosion rates along a climate and ecological gradient (Chile) to global observations, Earth Surf.

874 Dynam., 10 (1), 131-150, https://doi.org/10.5194/esurf-10-131-2022, 2022.

875   Schwanghart, W. and Scherler, D.: Short Communication: Topo Toolbox 2 – MATLAB-based

876   software for topographic analysis and modeling in Earth surface sciences, Earth Surf. Dynam., 2,

877   1–7, https://doi.org/10.5194/esurf-2-1-2014, 2014.

878   SERNAGEOMIN, Mapa Geológico de Chile: versión digital, Servicio Nacional de Geología y

879   Minería, Publicación Geológica Digital No. 4 [dataset], http://www.ipgp.fr/~dechabal/Geol-

880   millon.pdf, 2003.

881   Shobe, C. M., Tucker, G. E., and Anderson, R. S.: Hillslope-derived blocks retard river incision,

882   Geophys. Res. Lett., 43, 5070–5078, https://doi.org/10.1002/2016GL069262, 2016.

883   Sklar, L.S., and Dietrich, W.E.: Sediment and rock strength controls on river incision into

884   bedrock, Geology, 29, 1087–1090, https://doi.org/10.1130/0091-

885   7613(2001)029<1087:SARSCO>2.0.CO;2, 2001.

886   Sklar, L. S., Riebe, C. S., Marshall, J. A., Genetti, J., Leclere, S., Lukens, C. L., and Merces, V.:

887   The problem of predicting the size distribution of sediment supplied by hillslopes to rivers,

888   Geomorphology, 277, 31–49, https://doi.org/10.1016/j.geomorph.2016.05.005, 2017.

889   Sklar, L.S., Riebe, C.S., Genetti, J., Leclere, S. and Lukens, C.E.: Downvalley fining of hillslope

890   sediment in an alpine catchment: implications for downstream fining of sediment flux in

891   mountain rivers, Earth Surf. Proc. Land., 45(8), 1828-1845, https://doi.org/10.1002/esp.4849,

892   2020.

893   Small, E.E., Anderson, R.S., Repka, J.L., and Finkel, R.St.: Erosion rates of alpine bedrock

894   summit surfaces deduced from in situ 10Be and 26A1, Earth Planet. Sc. Lett., 150, 413-425,

895   https://doi.org/10.1016/S0012-821X(97)00092-7, 1997.

896 Stone, J.O.: Air pressure and cosmogenic isotope production, J. Geophys. Res. Solid Earth, 105,

897 B10, 23753-23759, https://doi.org/10.1029/2000JB900181, 2000.

898 Terweh, S., Hassan, M.A., Mao, L., Schrott, L., and Hoffmann, T.O.: Bio-climate affects

899 hillslope and fluvial sediment grain size along the Chilean Coastal Cordillera, Geomorphology,

900 384, 107700, https://doi.org/10.1016/j.geomorph.2021.107700, 2021.

901 Thaler, E.A. and Covington, M.D.: The influence of sandstone caprock material on bedrock

902 channel steepness within a tectonically passive setting: Buffalo National River Basin, Arkansas,

903 USA, J. Geophys. Res. Earth Surf., 121(9), 1635-1650, https://doi.org/10.1002/2015JF003771,

904 2016.

905 van Dongen, R., Scherler, D., Wittmann, H., and von Blanckenburg, F.: Cosmogenic 10Be in

906 river sediment: where grain size matters and why, Earth Surf. Dynam., 7, 393–410,

907 https://doi.org/10.5194/esurf-7-393-2019, 2021.

908 van Dongen, R.: Discharge variability and river incision along a climate gradient in central Chile.

909 PhD thesis. Potsdam, Germany, 2021.

910 Verdian, J.P., Sklar, L.S., Riebe, C.S. and Moore, J.R.: Sediment size on talus slopes correlates

911 with fracture spacing on bedrock cliffs: implications for predicting initial sediment size

912 distributions on hillslopes, Earth Surf. Dynam., 9(4), 1073-1090, https://doi.org/10.5194/esurf-9-

913 1073-2021, 2021.

914 von Blanckenburg, F., Hewawasam, T., and Kubik, P.W.: Cosmogenic nuclide evidence for low

915 weathering and denudation in the wet, tropical highlands of Sri Lanka, J. Geophys. Res., 109,

916 F03008, https://doi.org/10.1029/2003JF000049, 2004.

917   Zernitz, E.R.: Drainage patterns and their significance, J. Geol., 40 (6), 498-521,

918   https://doi.org/10.1086/623976, 1932.

919   **10   Tables**

920   Table 1. ^{10}Be cosmogenic nuclide sample data.

Sample ID	IGSN [a]	Sampling location [b]	Latitude (°N)	Longitude (°E)	Sample type [c]	^{10}Be conc. ±2σ (×10^5) (atoms g^{-1})	^{10}Be conc. normalized by SLHL ±2σ (×10^5) (atoms g^{-1}) [d]	^{10}Be production rate (spallation, atoms g^{-1} yr^{-1})	Site scaling factor [e]	Slope angle at sample location (°) [f]	Avg. boulder width / protrusion or fracture density [g]	No. chips taken for sample
							Nahuelbuta					
NB-BR1	GFRD1002U	PdA ridge 1	-37.826	-73.035	BR	8.25±0.56	2.92±0.20	11.41	2.82	18	7.83	20
NB-BR2	GFRD1002V	PdA ridge 2	-37.821	-73.034	BR	6.92±0.48	2.43±0.18	11.44	2.85	4	4.75	15
NB-BR3	GFRD1002W	PdA ridge 3	-37.819	-73.032	BR	5.18±0.40	1.86±0.14	11.15	2.78	3	2	15
NB-BR4	GFRD10029	PdA ridge 4	-37.825	-73.032	BR	3.85±0.28	1.36±0.10	11.46	2.84	16	4.78	15
NA3	GFEL10002	PdA slope	-37.826	-73.034	BR	6.55±0.46	2.38±0.16	11.25	2.75	25	4.43	30
NA4	GFEL10003	CdP	-37.817	-73.031	B	9.08±0.64	3.49±0.24	10.43	2.60	5	1.70 / 0.68	30
NA7	GFEL10006	CA ridge	-37.789	-72.998	B	10.28±0.72	3.65±0.26	11.3	2.81	10	1.52 / 1.00	10
NA8	GFEL10007	CA ridge	-37.789	-72.998	B	8.94±0.62	3.18±0.22	11.3	2.81	10	3.30 / 2.43	10
NA9	GFEL10008	CA ridge	-37.789	-72.998	B	7.57±0.54	2.69±0.18	11.3	2.81	10	0.64 / 0.19	10
NA11	GFEL1000A	CA slope	-37.790	-72.999	B	7.67±0.54	2.76±0.18	11.18	2.78	14	1.90 / 1.60	10
NA15	GFEL1000E	SPH slope	-37.807	-73.013	B	2.84±0.14	1.12±0.06	10.24	2.53	18	0.96 / 0.76	12
NA5	GFEL10004	CdP	-37.817	-73.031	S	2.32±0.20	0.89±0.08	10.43	2.60	5	N/A	N/A
NA10	GFEL10009	CA ridge	-37.789	-72.998	S	5.04±0.36	1.79±0.12	11.3	2.81	10	N/A	N/A
NA12	GFEL1000B	CA slope	-37.790	-72.999	S	4.27±0.32	1.54±0.12	11.18	2.78	14	N/A	N/A
							La Campana					
LC-BR2	GFRD1002X	CC slope	-32.938	-71.081	BR	1.83±0.22	1.38±0.16	5.75	1.33	39	N/A	15
LC2	GFEL1002J	CC ridge	-32.939	-71.081	B	0.92±0.18	0.59±0.12	6.25	1.55	9	0.95 / 0.54	10
LC4	GFEL1003V	CC slope	-32.938	-71.079	B	0.92±0.16	0.66±0.12	5.77	1.40	27	0.30 / 0.15	10
LC11	GFEL1000Q	CG ridge	-32.941	-71.074	B	1.21±0.14	0.76±0.08	6.42	1.59	13	1.32 / 0.70	10
LC13	GFEL1000S	CG upper slope	-32.94	-71.073	B	0.73±0.16	0.51±0.12	6.13	1.43	33	0.32 / 0.20	12
LC18	GFEL1000Z	CG lower slope	-32.937	-71.074	B	1.55±0.16	1.17±0.12	5.43	1.32	18	0.50 / 0.32	12
LC1	GFEL1002H	CC ridge	-32.939	-71.081	S	1.54±0.18	0.99±0.12	6.25	1.55	9	N/A	N/A
LC3	GFEL1003W	CC slope	-32.938	-71.079	S	1.03±0.18	0.74±0.12	5.77	1.40	27	N/A	N/A
LC12	GFEL1000R	CG ridge	-32.941	-71.074	S	0.88±0.08	0.55±0.06	6.42	1.59	13	N/A	N/A
LC14	GFEL1000T	CG upper slope	-32.940	-71.073	S	0.63±0.08	0.44±0.06	6.13	1.43	33	N/A	N/A
LC19	GFEL1000X	CG lower slope	-32.937	-71.074	S	1.84±0.14	1.39±0.10	5.43	1.32	18	N/A	N/A
							Santa Grácia					
SG8	GFEL10017	SGH ridge	-29.756	-71.166	B	5.94±0.42	4.17±0.30	5.72	1.42	10	1.10 / 0.80	10
SG9	GFEL10018	SGH ridge	-29.756	-71.166	B	4.70±0.34	3.30±0.24	5.72	1.42	10	0.38 / 0.12	10
SG11	GFEL1001A	SGH slope 1	-29.758	-71.166	B	3.56±0.26	2.61±0.20	5.56	1.36	21	1.30 / 0.87	9
SG22	GFEL1001M	SGH slope 2	-29.758	-71.166	B	3.85±0.30	2.83±0.22	5.56	1.36	22	0.37 / 0.24	11
SG37	GFEL1002T	ZH ridge	-29.740	-71.156	B	11.46±0.88	8.21±0.62	5.64	1.40	28	1 / 0.90	10
SG38	GFEL1002S	ZH ridge	-29.740	-71.156	B	7.84±0.56	5.62±0.40	5.64	1.40	28	0.10 / 0.12	10
SG10	GFEL10019	SGH ridge	-29.756	-71.166	S	2.58±0.22	1.81±0.16	5.72	1.42	10	N/A	N/A
SG12	GFEL1001B	SGH slope 1	-29.758	-71.166	S	2.39±0.18	1.75±0.14	5.56	1.36	21	N/A	N/A
SG23	GFEL1001N	SGH slope 2	-29.758	-71.166	S	2.10±0.16	1.54±0.12	5.56	1.36	22	N/A	N/A
SG36	GFEL1002U	ZH ridge	-29.740	-71.156	S	5.40±0.50	3.87±0.36	5.64	1.40	28	N/A	N/A

[a]Open access metadata: http://igsn.org/[insert IGSN number here]
[b]Sample locations: PdA: Piedra de Aguila, CdP: Casa de Piedas, CA: Cerro Anay, SPH: Soil Pit Hill, CC: Cerro Cabra, CG: Cerro Guanaco, SGH: Santa Gracia Hill, ZH: Zebra Hill..
[c]Sample type abbreviations: BR: bedrock, B: boulders, S: soil.
[d]Concentrations were normalized to SLHL (sea level high latitude) using a SLHL production rate of 4.01 atoms g-1 yr^{-1} (Borchers et al., 2016) and the site's scaling factor.
[e]Time constant spallation production rate scaling scheme of Lal (1991) and Stone (2000) ('St' in Balco et al., 2008), calculated taking topographic shielding into account.
[f]Local hillslope angles were calculated using a 12.5m DEM and an 8-connected neighbourhood method.
[g]Fracture density for bedrock (in meters) and width and protrusion measurements (in meters) for boulders. Values are averages of >10 measurements per sample site.

Table 2. Modelled denudation rates for soil and boulder samples using the first term of Eq. 1, and comparison of modelled and measured ^{10}Be concentrations for soil samples. Sample location abbreviations are described in the caption for Table 1.

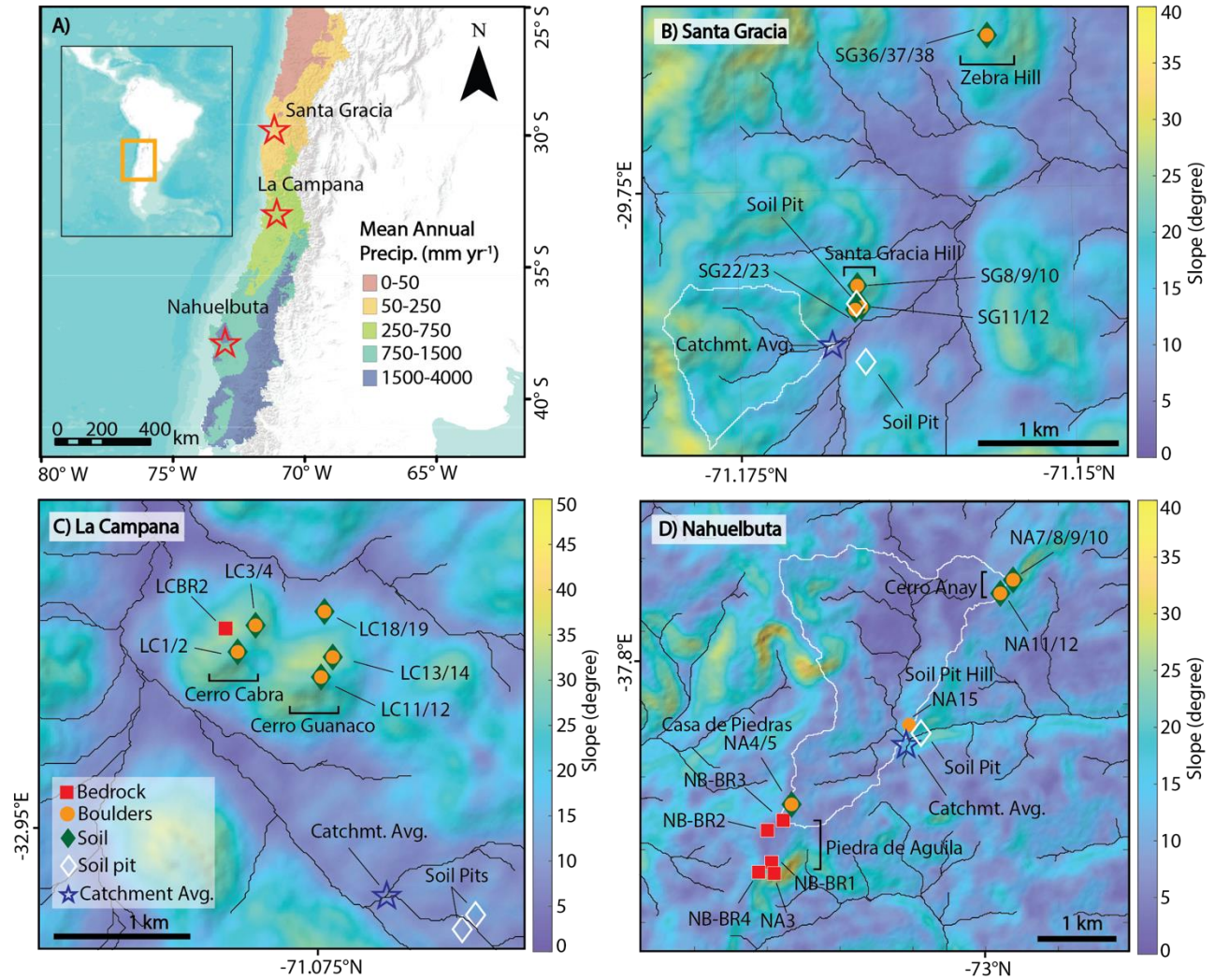| Sample location	Soil sample ID	Best-fitting modelled soil denudation range rate (ϵ_s) (m Myr^{-1})	Corresp. modelled range of ^{10}Be conc. ($\times 10^5$) (atoms g^{-1}) for soil (N_m)	Measured ^{10}Be conc. $\pm 2\sigma$ ($\times 10^5$) (atoms g^{-1})	Boulder sample IDs	Best-fitting modelled boulder denudation rate range (ϵ_b) (m Myr^{-1})	Differential erosion rate (boulder vs. soil; m Myr^{-1})	Time needed for boulder exposure (Kyr)
Nahuelbuta								
CdP	NA5	15-20	3.61-4.75	2.32±0.20	NA4	10-15	5	136
CA ridge	NA10	15-20	3.89-5.12	5.04±0.36	NA7, NA8, NA9	10-15	5	200, 486, 38
CA slope	NA12	18-20	3.84-4.25	4.27±0.32	NA11	15-18	2.5	640
La Campana								
CG ridge	LC12	70-90	0.54-0.69	0.88±0.08	LC11	40-60	30	23
CG upper slope	LC14	120-140	0.32-0.37	0.63±0.08	LC13	80-120	30	7
Santa Gracia								
SGH ridge	SG10	12-15	2.77-3.41	2.58±0.22	SG8, SG9	10-12	2.5	320, 48
SGH slope 1	SG12	19-21	1.94-2.13	2.39±0.18	SG11	18-20	1	870
SGH slope 2	SG23	19-21	1.94-2.13	2.10±0.16	SG22	18-20	1	240
ZH ridge	SG36	6.5-7.5	4.78-5.45	5.40±0.50	SG37, SG38	4-5.5	2.25	400, 53

11 Figures

Figure 1. Field site locations and features. A) Map of mean annual precipitation in central Chile, with field sites marked by red stars. Precipitation data from the CR2MET dataset, by the Center for Climate and Resilience Research (CR^2) (Boisier et al., 2018), provides an average for the time period 1979-2019. World Terrain Base map sources are Esri, USGS, NOAA. B-D: Slope and hillshade maps from 12.5-m ALOS PALSAR digital elevation models, of B) Santa Gracia (SG), C) La Campana (LC), and D) Nahuelbuta (NA). Sample locations and sample names are shown, with symbol shape and color indicating the sample type (see legend in lower left panel). White outlines delineate the catchments from which the catchment average sample (star) was taken (the catchment from La Campana does not fit within the bounds of the map and therefore is not shown). Black lines indicate streams. Soil pit sample data are from Schaller et al. (2018), and catchment average sample data are from van Dongen et al. (2019).

Figure 2. Field photos showing the various surfaces sampled, including bedrock, boulders and soil. Figure panels are grouped by field site. A: Nahuelbuta, A1) Bedrock (sample NB-BR1). A2) Fractured bedrock, in transition between unfractured bedrock and boulders (sample NB-BR2). A3) Smaller boulders surrounded by soil (sample NA7). B: La Campana, B1) Bedrock (sample LC-BR2). B2) Bedrock transitioning to large boulders and soil. B3) Boulders and soil on a hillside (samples LC13 and LC14). C: Santa Gracia, C1) Boulders on Zebra Hill delineated by fractures. C2) Large boulders on the ridge of Santa Gracia Hill (sample SG8). C3) Soil with minimal boulders on the slope of Santa Gracia Hill (samples SG22 and SG23).

46
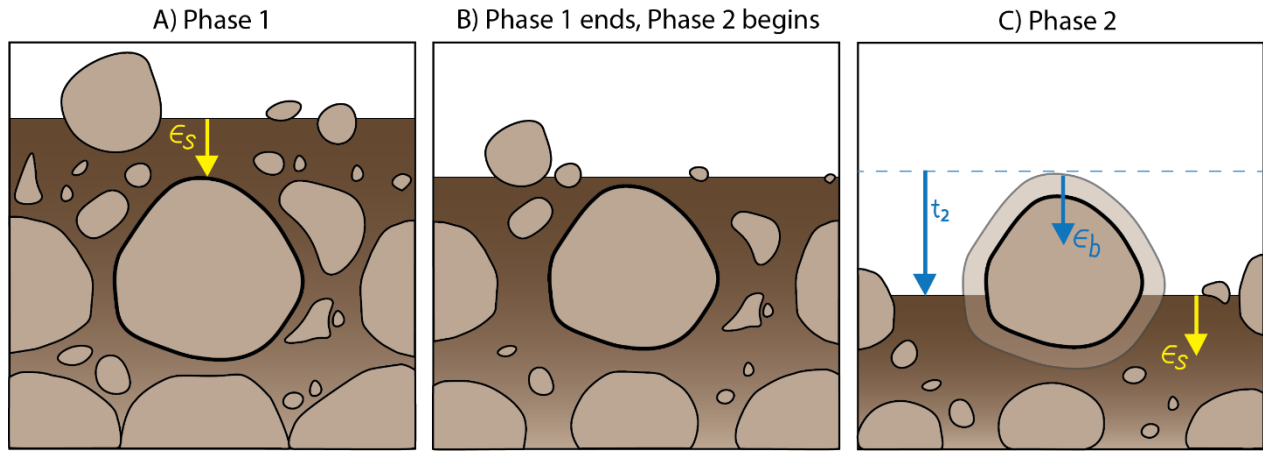
Figure 3. Schematic image showing the process of boulder exhumation. A) Overview of the setting: a mixed soil- and bedrock- covered hillslope where sediment size decreases with decreasing fracture spacing. B) During phase 1, the boulder is buried, and accumulates nuclides at a rate governed by the soil denudation rate, ϵ_s. C) Phase 1 ends when the boulder breaches the soil surface. D) During phase 2, the boulder itself is eroding at a rate of ϵ_b, and the surrounding soil continues to denude at a rate of ϵ_s. Phase 2 lasts for a time period t_2 that ends with our sampling.
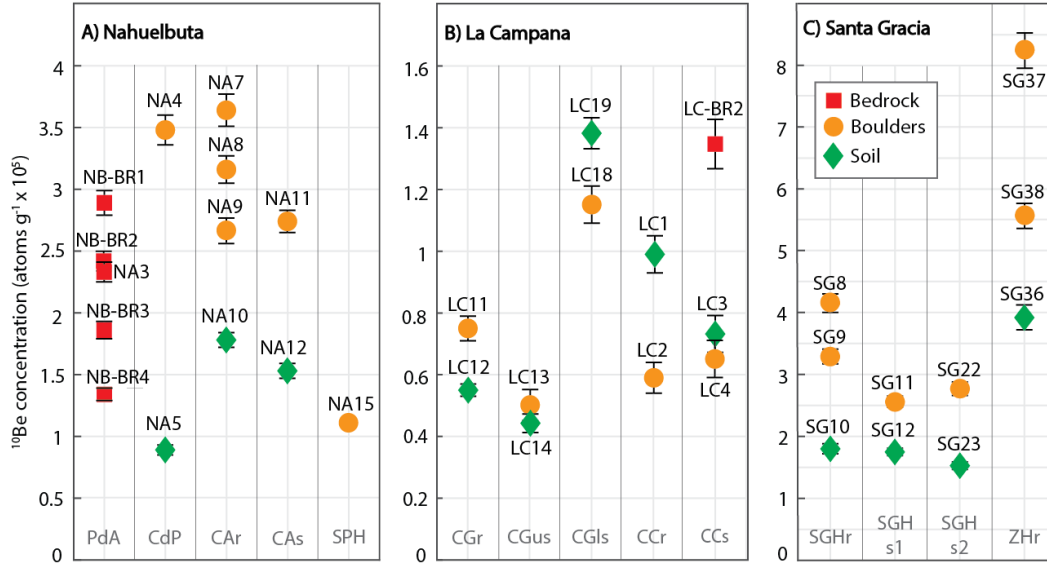
Figure 4. Measured ^{10}Be concentrations normalized to reference production rate at sea-level high latitude for A) Nahuelbuta, B) La Campana, and C) Santa Gracia; note different scales of y-axes. X-axes are not numerical but rather show the sampling locations, also reported in Table 1. Labels next to data points provide sample IDs, also reported in Table 1. Gray labels at the bottom of panels are the sample locations. PdA: Piedra de Aguila, CdP: Casa de Piedas, CAr: Cerro Anay ridge, CAs: Cerro Anay slope, SPH: Soil Pit Hill, CGr: Cerro Guanaco ridge, CGus: Cerro Guanaco upper slope, CGls: Cerro Guanaco lower slope, CCr: Cerro Cabra ridge, CCs: Cerro

Cabra slope, SGHr: Santa Gracia Hill ridge, SGHs1: Santa Gracia Hill slope 1, SGHs2: Santa Gracia Hill slope 2, ZHr: Zebra Hill ridge.
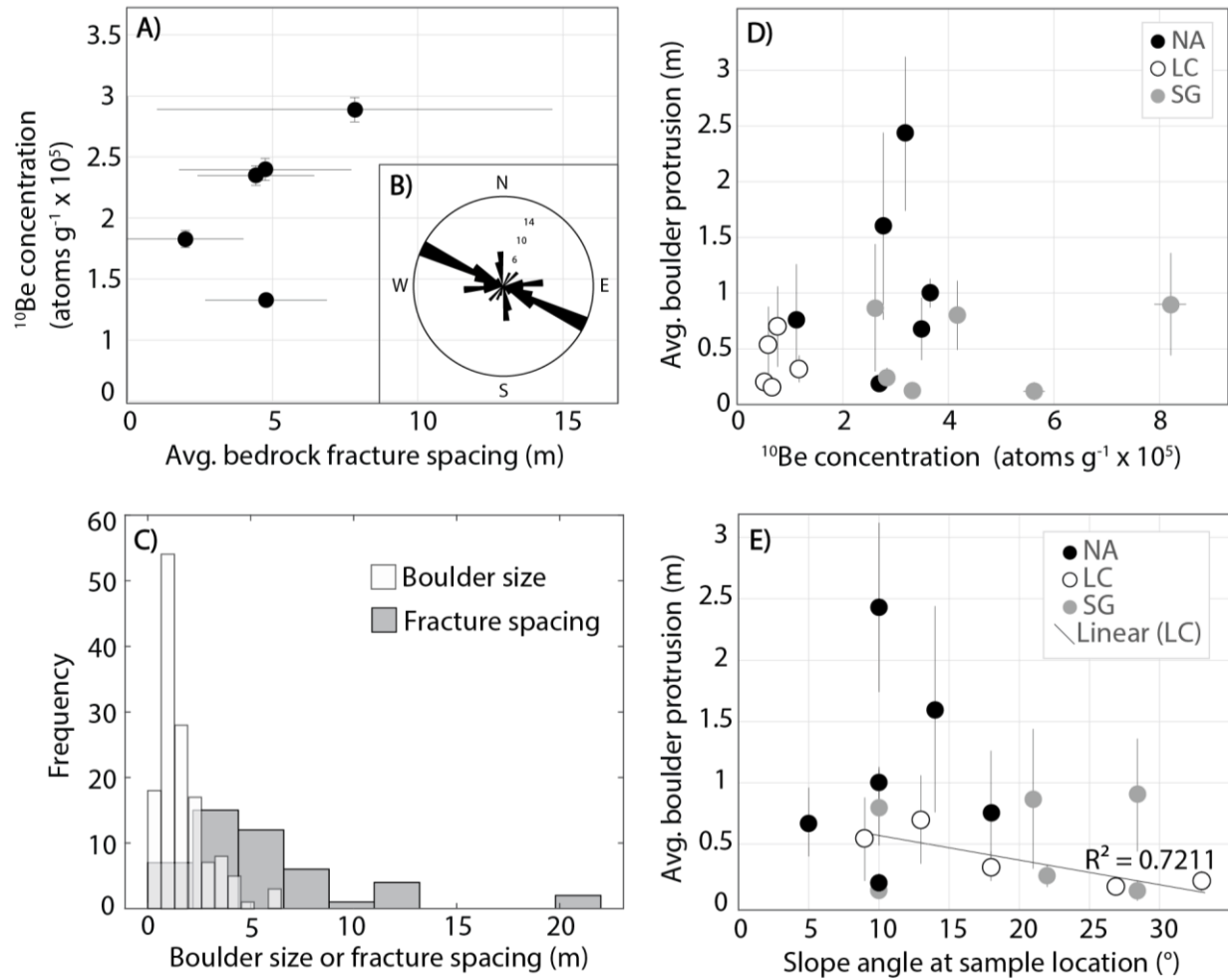

Figure 5. A) Average bedrock fracture spacing (NA only), plotted against measured ^{10}Be concentrations normalized to the reference production rate at sea-level high latitude. Error bars represent the standard deviation of all fracture spacing measurements for each location. B) Rose diagram showing bedrock fracture orientations measured in the field in NA (same fractures as panel A). C) Measurements of individual fracture spacing and individual boulder sizes, where boulder size is the average of the x and y axes of each boulder and the z axis is the protrusion height. D) Average boulder protrusion height plotted against measured ^{10}Be concentrations normalized to reference production rate at sea-level high latitude for each field site. Error bars represent the standard deviation of all boulder protrusion height measurements for each location. E) Average boulder protrusion height plotted against hillslope angle. A linear regression model is fit through LC datapoints.
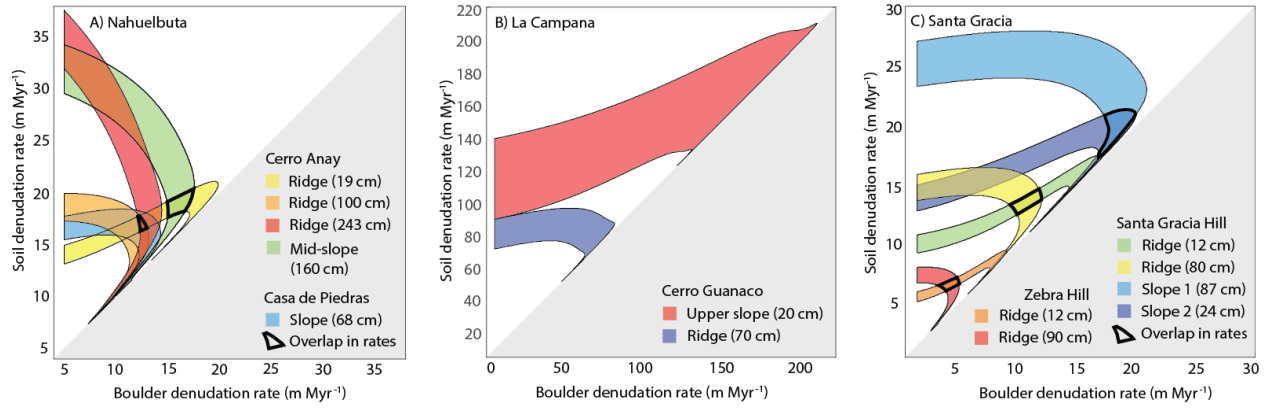
Figure 6. Range of best fitting combinations of modelled soil and boulder denudation rates in A) Nahuelbuta, B) La Campana, and C) Santa Gracia according to Eq. 1. Each color band corresponds to an amalgamated boulder sample, listed in the legend along with the average protrusion height of the boulders. Areas where best fitting denudation rates overlap for samples from the same location are highlighted by a black outline. The gray areas are forbidden fields, as by assumption, boulder denudation rates have to be lower than soil denudation rates, otherwise there would be no boulder protruding above the soil surface.
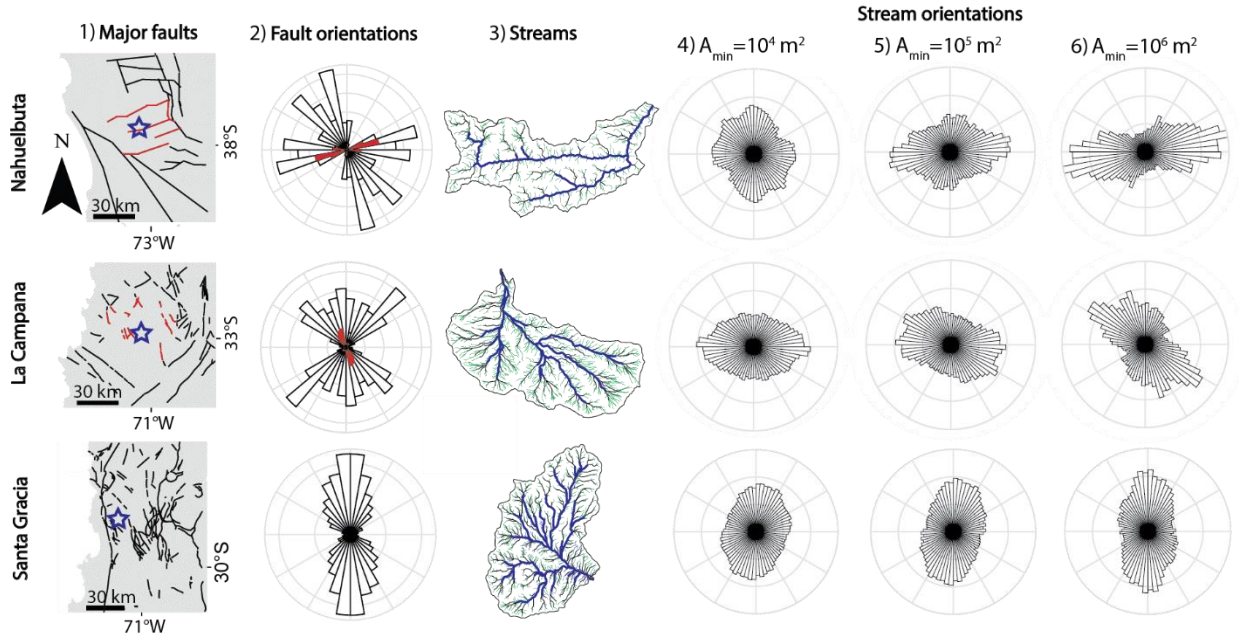

Figure 7. Rose diagram plots and maps showing fault and stream orientations for Nahuelbuta (top row), La Campana (middle row), and Santa Gracia (bottom row). For each field site, the columns show from left to right: (1) major faults digitized from geological map (SERNAGEOMIN, 2003), within ~50 km (black) and ~25 km (red, NA and LC only) of the sampling site (blue star); (2) rose diagram of fault orientations from the maps in column 1, constructed using 100 m long, straight fault segments and 36 bins, with orientations of faults <25 km from NA and LC in red; (3) a map of the studied catchments and the drainage network, with green, black, and blue streams indicating minimum upstream areas (A_{min}) of 10^4, 10^5, and 10^6 m^2, respectively, derived

from one-meter resolution LiDAR DEMs (Kügler et al., 2022).; (4-6) rose diagrams (72 bins) of stream orientations for different A_{min}. All maps and rose diagrams are oriented with the top being north.
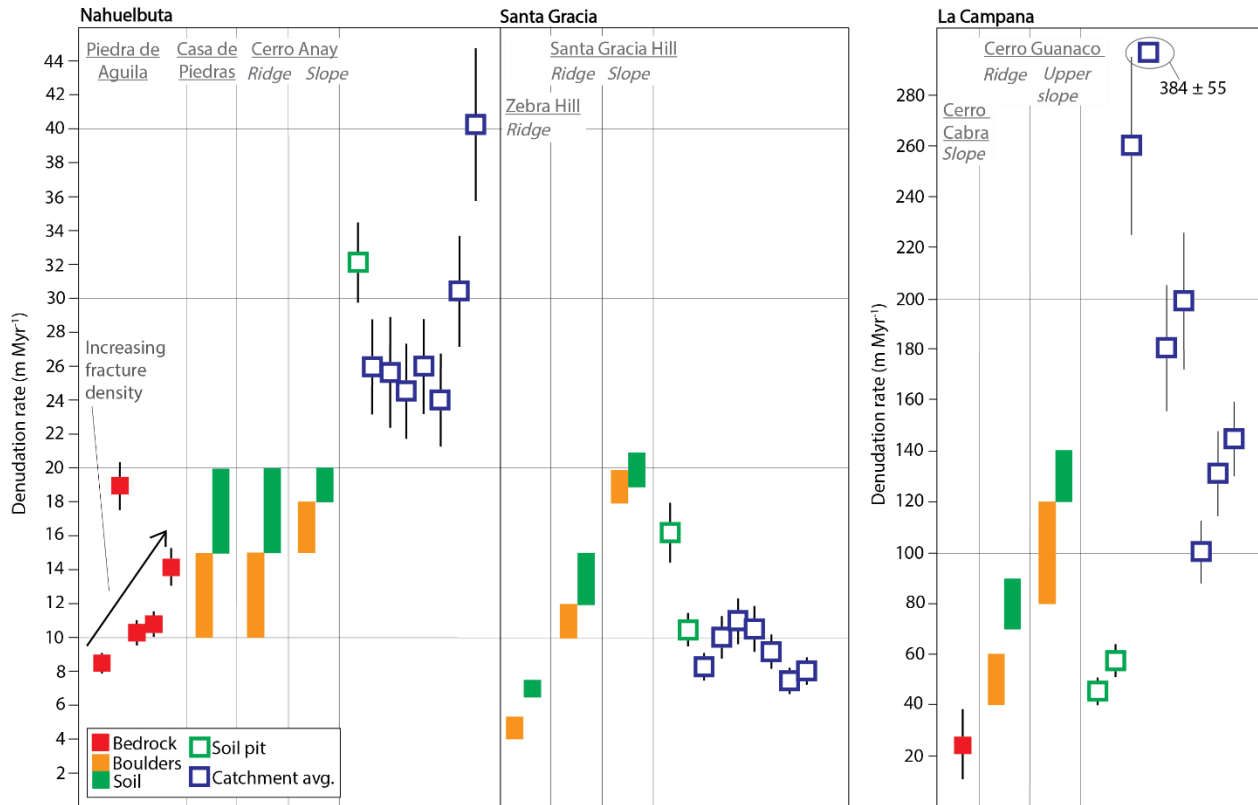

Figure 8. Overview of new and previously published denudation rates (data from this study are shown by solid symbols and previously-published data are shown by hollow symbols). Soil pit data is from Schaller et al. (2018), and catchment average data is from van Dongen et al. (2019). Catchment average denudation rates from various sediment grain sizes (from left to right for each field site: 0.5-1, 1-2, 2-4, 4-8, 8-16, 16-32, and 32-64 mm). Bedrock denudation rates are calculated using the CRONUS online calculator v2.3 (Balco et al., 2008). Boulder and soil denudation rates are estimated using our model and reflect the most plausible denudation rates as described in section 5.1.2. Denudation rates for each location within a field site are separated by thin gray bars, and locations are labeled at the top of the chart. Samples that were not included in the model (one sample from Nahuelbuta and 3 samples from La Campana) are also not included here.
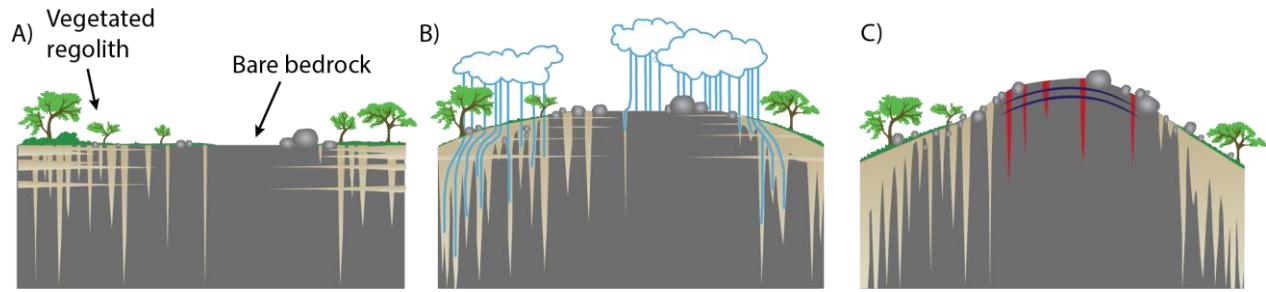
Figure 9. Schematic illustration showing influence of bedrock fractures on landscape evolution. (A) Bedrock with different fracture densities is to different degrees infiltrated by rain and ground water, which leads to differences in chemical weathering, soil formation and vegetation growth, resulting in different hillslope sediment sizes. (B) Differential denudation between highly fractured and less fractured areas induce relief growth under slow but persistent uplift, which further promotes spatial gradients in chemical weathering, hillslope sediment size, and denudation. (C) Growing relief increases topographic stresses and formation of new fractures (red) at topographically high positions (e.g. St. Clair et al., 2015) as well as non-topographic surface-parallel fractures (dark blue) (e.g. Martel, 2011), and steeper slopes allow for transportation of boulders, shown rolling down the slopes on either side.